Main Manuscript for

Oncogenic mutations on Rac1 affect global intrinsic dynamics underlying GTP and PAK1 binding

Running Title: Rac1 mutations affect intrinsic dynamics

Saliha Ece Acuner[a,b], Fidan Sumbul[a,c], Hamdi Torun[d,*], Turkan Haliloglu[a,*]

[a]Department of Chemical Engineering and Polymer Research Center, Bogazici University, 34342 Istanbul, Turkey.

[b]Present address: Department of Bioengineering, Istanbul Medeniyet University, 34700 Istanbul, Turkey. E-mail: ece.ozbabacan@medeniyet.edu.tr

[c]Present address: Aix-Marseille Univ, INSERM, CNRS, U1067, 13009, Marseille, France. E-mail: fidan.sumbul@inserm.fr

[d]Department of Mathematics, Physics and Electrical Engineering, Northumbria University, NE1 8ST Newcastle, UK.

*Corresponding Authors: Turkan Haliloglu and Hamdi Torun

Phone: +90 (212) 359 7002. Fax: +90 (212) 257 5032. E-mail: halilogt@boun.edu.tr

Phone: +44 (191) 227 4746. Fax: +44 (191) 227 3903. E-mail: hamdi.torun@northumbria.ac.uk

SEA and FS contributed equally to this work

ORCID IDs: SEA: 0000-0003-0336-0645; FS: 0000-0002-2250-4280; HT: 0000-0002-7882-286X; TH: 0000-0002-1279-5803

This PDF file includes: Main Text, Figures 1 to 5, and Tables 1 to 2

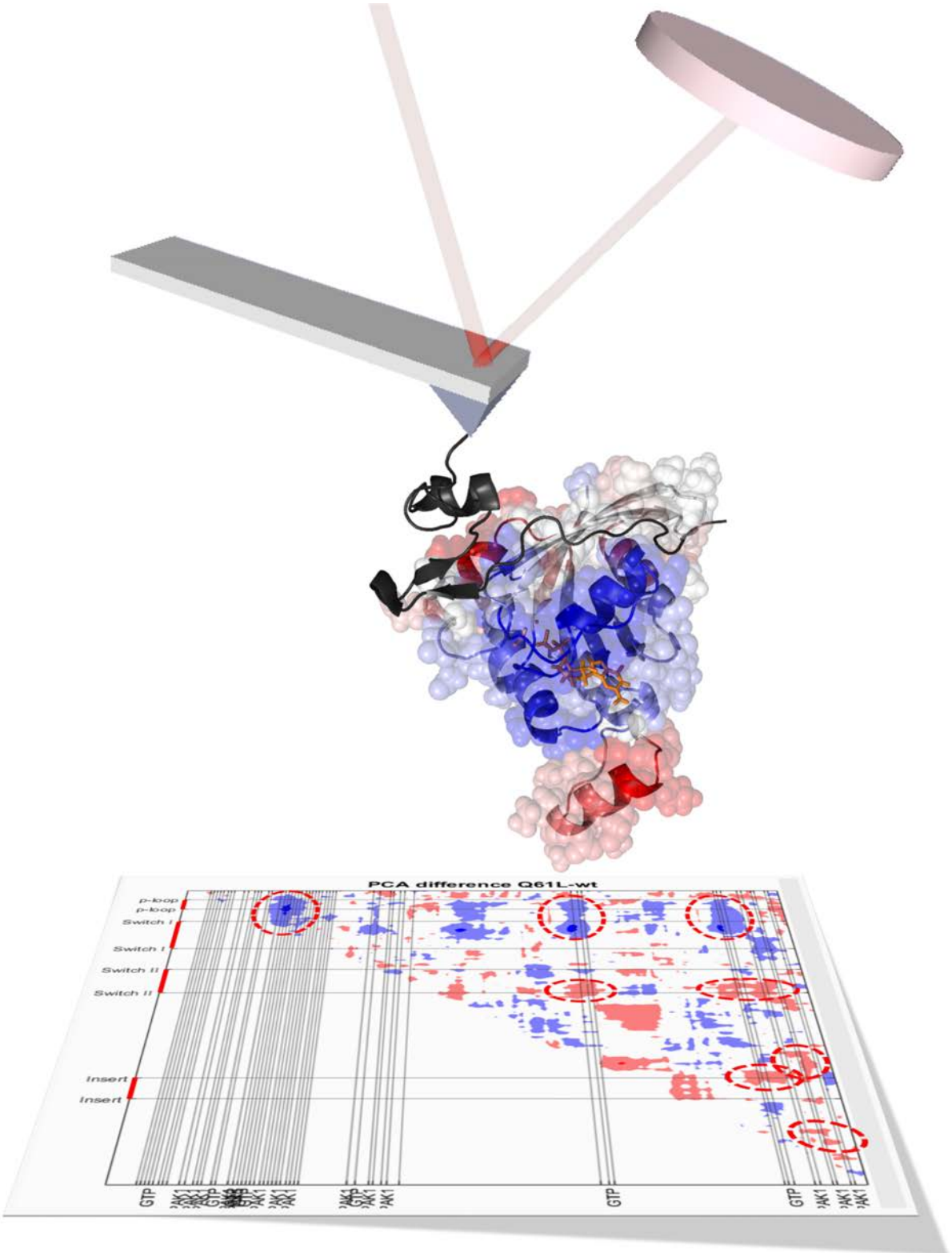
PCA difference Q61L-wt
p-loop
p-loop
Switch I
Switch I
Switch II
Switch II
Insert
Insert
GTP
GTP
GTP

Abstract

Rac1 is a small member of Rho GTPase family. One of the most important downstream effectors of Rac1 is a serine/threonine kinase, p21-activated kinase 1 (PAK1). Mutational activation of PAK1 by Rac1 has oncogenic signaling effects. Here, while we focus on Rac1-PAK1 interaction by atomic force microscopy (AFM)-based single molecule force spectroscopy (SMFS) experiments, we explore the effect of active mutations on the intrinsic dynamics and binding interactions of Rac1 by Gaussian Network Model (GNM) analysis and Molecular Dynamics (MD) simulations. We observe that Rac1 oncogenic mutations are at the hinges of three global modes of motion suggesting the mechanical changes as potential markers of oncogenicity. Indeed, the dissociation of wild-type Rac1-PAK1 complex shows two distinct unbinding dynamic states that are reduced to one with constitutively active Q61L and oncogenic Y72C mutant Rac1 as revealed by SMFS experiments. Q61L and Y72C mutations change the mechanics of Rac1-PAK1 complex by increasing elasticity of the protein and slow down the transition to the unbound state. On the other hand, Rac1's intrinsic dynamics reveal more flexible GTP and PAK1-binding residues on Switch I and II with Q61L, Y72C, oncogenic P29S and Q61R and negative T17N mutations. The cooperativity in the fluctuations of GTP-binding sites around p-loop and Switch I decreases in all mutants, mostly in Q61L, while some PAK1-binding residues display enhanced coupling with GTP-binding sites in Q61L and Y72C and within each other in P29S. The predicted binding free energies of the modeled Rac1-PAK1 complexes show that the change in the dynamic behavior likely means a more favorable PAK1 interaction. Overall, these findings suggest that the active mutations affect intrinsic functional dynamic events and alter the mechanics underlying the binding of Rac1 to GTP and upstream/downstream partners including PAK1.

Statement of Significance

Rac1 acts as a binary molecular switch between the GTP-bound active and GDP-bound inactive states, and has important roles in oncogenic signaling. Through an integrated computational and experimental approach at single-molecule level, we explore the mutation-dependent dynamic regulation of the small GTPase Rac1 in atomistic detail. Here, we elucidate that active mutations P29S and Q61R as well as Q61L and Y72C affect the intrinsic dynamic events underlying the binding of Rac1 to GTP and upstream/downstream partners through an allosterically regulated interplay between important functional regions on Rac1. The findings here posit an intrinsic dynamic mechanism that could be utilized in drug design efforts.

Keywords

Protein Dynamics, Allostery, Hinges, Molecular Simulations, Gaussian Network Model, AFM, Single Molecule Force Spectroscopy

Main Text

Introduction

Rac1 (Ras-related C3 botulinum toxin substrate 1) is an important GTPase in all eukaryotic organisms, regulating cytoskeletal organization and cell motility in response to extracellular signals (1, 2). Associated with the plasma membrane, Rac1 acts as a binary molecular switch between the GDP-bound inactive (OFF) and GTP-bound active (ON) states (3). The activation/inactivation cycle is regulated by guanine nucleotide exchange factors (GEFs), GTPase activating proteins (GAPs) and GDP-dissociation inhibitors (GDIs) (Figure 1). GEFs activate Rac1 to transmit an incoming signal through a series of fast reactions: catalysis of GDP release, transient stabilization of the nucleotide-free state during GDP/GTP exchange and catalysis of GTP binding. GAPs inactivate Rac1 by accelerating the weak intrinsic hydrolysis of GTP to GDP through stabilization of the charged intermediate and reduction of the activation barrier for hydrolysis (3-6). On the other hand, the negative regulators of Rho family, namely RhoGDIs, inhibit both nucleotide dissociation of GDP and hydrolysis of GTP, and can help Rac1 release from the membrane (Figure 1) (7). GDIs interact with both GDP- and GTP-bound GTPases, with a lower affinity towards the latter (8). One of the most important downstream effectors of Rac1 is PAK1 (p21-activated kinase 1, belonging to Pak family) (9). PAKs are serine/threonine kinases that interact with multiple partners to regulate essential cellular processes such as cytoskeletal regulation, motility and apoptosis (10).

Rac1 is involved in various steps of cancer including its “player” role in cancer cell migration and invasion, as well as its “driver” role in regulating tumor metastasis and progression (11-19). In this study, we focus on the oncogenic mutational positions P29, Q61 and Y72 as well as one negative control position T17 (Figure 2). Rac1 is the third proto-oncogene that mutates most frequently in melanoma (after BRaf and NRas, identified in 9% of UV light related melanomas) with the hotspot somatic missense mutation P29S (19-22). P29S is a fast-recycling (i.e., spontaneously active) mutant with gain-of-function property as it increases the ability to switch from the inactive to active state through enhanced GDP/GTP exchange. Without losing its GTPase function, this increases the binding events to downstream effectors (20, 21). Q61R is a prostate cancer-associated gain-of-function mutation in Rac1 (23-25) and potently induces Rac1 activation as in P29S (26). Q61L, however, is a constitutively active loss-of-function mutation, which is oncogenic in KRas but not in Rac1. Q61L prevents GTPase activity by blocking GAP-stimulated hydrolysis of GTP to GDP (4). Fast-recycling mutants might be more efficient oncogenic drivers than constitutively active mutants due to their ability to mimic normal signaling (19). Y72C is a rare oncogenic mutation related to liver carcinoma listed in COSMIC database (23). Y72C is considered as a case study here; due to a lack of information about the functional mechanism leading to its oncogenicity. T17N, used as a negative test case, is a dominant-negative mutation on p-loop that prevents GTP binding and reduces GDP binding (2). Thus, T17N is in either nucleotide free or inactive state, causing competitive binding to GEFs with higher affinity than the wild-type to block activation (27). Both dominant-negative and constitutively active mutants have important roles in the relation of Rho GTPase family (including Rac1) with oncogenesis (27).

There are four main functional sites in Rac1 protein: insert region, p-loop, and switch loops (Switch I and II) (Figure 2A). Insert region is specific to Rho subfamily and regulates signaling activity by interacting with GEFs (28), GDIs (29) and downstream effectors (30). Although being distant to the binding site, insert region was shown to be important in GDI binding, which leads to the inhibition of GDP dissociation by stabilizing the bound nucleotide (29, 31). The p-loop coordinates the γ-phosphate of the guanine nucleotides (GDP and GTP) and Mg^{2+} ion during the nucleotide binding of Rac1 (28). The p-loop was also shown to have a role in GAP binding along with the switch loops (32). Switch I, also known as the “effector region”, is mainly responsible for the interaction of Rac1 with downstream effectors (e.g. PAK1 and MLK3). Switch I also includes some important nucleotide binding residues. Switch II is important for the specific recognition and activation of Rac1 by GEFs and/or inactivation by GAPs (33). Overall, the residues on both switch loops participate in upstream and downstream signaling through PAK1-, GAP-, GEF- and GDI-binding, thus having a crucial role in Rac1 activity (28, 33).

The conformation of the switch loops changes dramatically upon GTP binding with hydrogen bonds forming between the γ-phosphate and residues T35 (Switch I) and G60 (Switch II) (7). During GTP

hydrolysis, it is important to position T35 such that the affinity for the nucleotide binding is enhanced via the coordination of the main chain carbonyl of T35 with both the Mg^{2+} ion and the γ-phosphate (7). Mg^{2+} is considered as a "gatekeeper" of nucleotide exchange as it is involved in the regulation of both nucleotide binding and hydrolysis kinetics. In addition, Mg^{2+} stabilizes both nucleotide-bound states of Rac1. Its coordination with T17, T35 and D57 can keep Rac1 in the GDP-bound inactive state, whereas both GDP and Mg^{2+} are destabilized during GEF binding and activation of Rac1 (34, 35). On the other hand, Mg^{2+} binding enhances the intrinsic GTP hydrolysis rates up to 10-fold and its presence significantly increases the rates of the RhoGAP-catalyzed hydrolysis reactions (35). So, new interactions introduced with GTP binding changes the structure and dynamics of the switch loops, which are unstructured or highly flexible otherwise (7). Moreover, the switch loops display significantly reduced flexibility upon effector binding (36).

Exploring the structural and dynamic alterations underlying functional variations with disease-related genetic mutations is of significant interest towards drug development in cancer treatments (37). Active mutations likely change the dynamics of OFF/ON states as well as the transition pathway in between, shifting the populations in favor of certain states. The computation of conformational heterogeneity of mutant GTPases (e.g. Ras and Rac1) is important yet challenging since the entire conformational transition pathway can only be observed using extended classical Molecular Dynamics (MD) simulation timescales (microseconds or milliseconds) or accelerated MD simulations (38-40). In the scope of this paper, we focus on the GTP-bound (ON) state of Rac1 and the effects of active mutations on its intrinsic dynamics and binding interactions, particularly PAK1-binding. Two of these Rac1 mutants already known to be fast-recycling (spontaneously active, P29S) and constitutively active (Q61L) have increased population in the GTP-bound state (41, 42).

Binding is an intrinsic dynamic phenomenon. The cooperative motion favored by the intrinsic dynamics has been shown to have close similarity to structural changes observed during binding actions, i.e. global motions underlie functional structural changes in different states (liganded, complexed, or free) observed in experiments (43-46). These conformational motions are usually energetically favorable fluctuations driven by low frequency global modes. The ligands and oligomeric interactions modulate the equilibrium conformation by affecting the energetic profile along these few global modes, which trigger allosteric interactions. The association of active mutations with the three global dynamic modes that we show in Rac1 provides us with a mechanistic framework. While we focus on the Rac1–PAK1 interaction by atomic force microscopy (AFM)-based single molecule force spectroscopy (SMFS) experiments, we quest the response of internal dynamics of Rac1 to the active mutations with respect to the intrinsic binding behavior by MD simulations, and the structural modeling of wild-type and mutant Rac1s in complex with PAK1.

Materials and Methods

Experimental Methods

We performed AFM-based SMFS experiments to probe the unbinding dynamics of Rac1 against PAK1. Specifically, we measured the single-molecular interactions of wild-type as well as T17N, Q61L and Y72C mutants of Rac1 with PAK1 (we only used p21-binding domain of PAK1 in our experiments). In this method, the free energy landscape (FEL) of the molecular pair can be perturbed by directly applying force on individual molecules so that the influence of force on transition rates from one state to another can be measured. Preparation and immobilization of molecules, the experimental setup and data interpretation are explained in detail in Supplemental Information. The experimental setup and the multi-step functionalization of AFM tips and surfaces are depicted in Figure 3A (the details are explained in Supplemental Information). We assessed the specificity of the measured forces via three different control experiments (see Figure S1). We determined the most probable rupture force of the Rac1-PAK1 complexes at a given loading rate by calculating the median of the force histograms (for the details of data interpretation see the corresponding sections and Equation S1 in Supplemental Information).

Computational Methods

We mapped the known oncogenic mutations on Rac1 using the data in COSMIC and cBioPortal (23-25) to the wild-type Rac1 structure (PDB ID: 3th5) to observe the extent of the association of the disease-related mutations with the predicted global hinge sites considering three slowest modes using the Gaussian Network Model (GNM) (47, 48) (Figure 2D-F). Then, we selected the case study mutations and performed molecular-dynamics (MD) simulations for the wild-type and mutant Rac1 structures. The starting structures for the simulations are: the GTP-bound wild-type Rac1 (PDB ID: 3th5), P29S mutant Rac1 (PDB ID: 3sbd), Q61L mutant Rac1 (PDB ID: 4gzl), Q61R, Y72C mutant Rac1 (*in silico*) and also nucleotide free T17N mutant Rac1 (PDB ID: 3b13). We performed a 2.4 μs-long simulation including four (100 ns-long) parallel runs for the wild-type and five mutant Rac1 structures. We analyzed MD sampled ensemble of conformations in detail to identify and characterize the shift and variations between the wild-type and mutant Rac1 structures (See Table S1 and SI for details). We also modelled the complexes of the representative Rac1 conformations in each simulated system (wt, P29S, Q61L, Q61R, Y72C and T17N Rac1) with the available PAK1 structure (PDB ID: 1e0a) to complement the MD analysis and results (Table S2).

Results and Discussion

Mechanistic role of active mutations at global hinge sites

Disease related genetic mutations are likely to be associated with the global hinge sites that coordinate collective functional motion of Rac1 (46, 49, 50). We observe about 90% (61 out of 68) of the Rac1 oncogenic mutations at/near the principle hinge axes of the three slowest, i.e. global, modes of motion revealed by GNM, providing a dynamic rationale for not being sporadic in the structure (Figures 2C-F and S2), as observed previously (50).

We selected three of the oncogenic mutational positions (P29, Q61 and Y72) and one negative control position (T17) that are at/near these global hinge sites, at functional and binding sites of Rac1 and have known diverse effects on Rac1 function. These mutations are namely the dominant negative T17N, constitutively active Q61L and oncogenic P29S, Q61R and Y72C. Their positions on Rac1 and their proximity to the binding sites are as follows (Figure 2A-C): T17 on p-loop is a nucleotide binding residue interacting also with Mg^{2+} ion. P29 on Switch I is close to both GTP- and PAK1-binding region. Q61 on Switch II is a GEF-binding residue and close to GTP-, GAP-, PAK1 and GAP-binding residues. Lastly, Y72 on Switch II is close to PAK1-binding residue L70.

The effects of perturbations introduced by T17N, P29S, Q61L/R and Y72C mutations on the intrinsic dynamics of Rac1 by concentrating on the binding regions of Rac1 with GTP, upstream proteins (GEF, GDI and GAP) and downstream partner PAK1, are analyzed through extensive MD simulations. Particularly, the effect of Q61L and Y72C mutations specifically on Rac1-PAK1 binding mechanics has been subjected to a more elaborate analysis with single molecule force spectroscopy experiments using AFM and molecular modeling of the complex structure.

GTP loaded wild-type Rac1-PAK1 is a multistate complex

The measured force curves with AFM-based SMFS experiments (experimental setup depicted in Figure 3A) initially show a characteristic increasing force as a result of flexible stretching of polyethylene glycol (PEG) linker and then a sudden decrease in force due to the unbinding of Rac1-PAK1 complex (Figure 3B). We observe similar probability of adhesion in the GTP-loaded wild-type (wt), Q61L and Y72C Rac1-PAK1s under similar experimental conditions. It is, however, significantly lower for the nucleotide-free dominant-negative T17N Rac1-PAK1, which indicates a loss of binding ability of Rac1 to PAK1 with T17N which we used as a negative control case (Figure 3C). A bimodal distribution in the unbinding forces of wt Rac1-PAK1 appears within the range of measured loading rates, while it becomes unimodal with Q61L and Y72C. The bimodal distribution of the unbinding forces can be explained by the existence of two different states in the mechanics of wt Rac1-PAK1 (namely state 1 and state 2 for the lower and higher unbinding forces, respectively). These two states may correspond to different conformational and/or dynamical states of both Rac1 itself or Rac1-PAK1

complex structure. The measured rupture forces between 200-300 pN of Rac1-PAK1, will be referred as state 1, are observed only in wt Rac1. The forces observed in this state are even higher than the unfolding forces of Ig domains from cardiac titin (~200pN) at similar loading rates (51) (Figures 3D, triangles). The measured rupture forces of wt Rac1-PAK1 in the range of 20-200 pN also appear for the Q61L and Y72C Rac1-PAK1s at similar loading rates (Figures 3D-F and S4). This state will be refereed as state 2. Higher rupture forces indicate that state 1 of wt Rac1 is mechanically a more stable but probabilistically less sampled state (Figure S3A).

Change in the mechanics of Rac1-PAK1 complex upon selected active mutations

The dynamic force spectrum obtained from the most probable rupture forces at each loading rate interval for wt, Q61L, Y72C Rac1-PAK1s are shown in Figure 3D-F (see also Figure S4), respectively. The linear increase in rupture forces with logarithmically increasing loading rates is in agreement with phenomenological Bell-Evans model (52, 53). Although a single barrier model is sufficient to describe the unbinding free energy landscape (FEL) of state 1 of wt Rac1-PAK1 dissociation, the unbinding FEL of state 2 of wt, Q61L, Y72C Rac1-PAK1s possess multiple barriers in the range of measured loading rates. The outer and inner barriers are dominant respectively at low and high loading rates.

Table 1 displays the natural dissociation rate (k_{off}) and the effective distance to the transition state (x_β) for each case according to the Bell-Evans model. With multiple energy barriers, only the rate-limiting slowest step (the outer barriers with significantly lower k_{off} values than the inner barriers) is considered for further discussion. The lower the dissociation rate is, the higher the activation energy barrier in the unbinding FEL and the longer the lifetime of the complex are. As such, the unbinding rate of the mutants shifts towards state 1 while unbinding forces resemble state 2 of wt Rac1 in the dynamic force spectrum.

The distance from the ground state (x_β) to the transition state along the unbinding pathway also changes with mutations (Table 1). Higher the distance to the transition state, the wider the energy barrier. As the FEL is a rough surface, wider barrier is directly related to the abundance of intermediate states. Alternatively, higher distance to the transition states may also imply a higher elasticity of the protein itself as the protein may extend as the ligand pulled away (54). Relatively shorter distances for both states of wt Rac1-PAK1 interaction suggest a highly structurally coordinated unbinding process of the complex. Higher distance to the transition state observed in Q61L and Y72C mutants indicates an increased elasticity at either locally in binding interface, which might be related to the variable spatial accessibility of the Rac1 binding sites, or globally in the whole Rac1 structure.

We thus anticipate that there should be a change in the internal dynamic cooperativity in Rac1-PAK1 complex with the mutations, which we explore with the intrinsic dynamics of Rac1 by MD simulations in the following sections.

Intrinsic dynamics of Rac1 revealed by MD simulations

Binding is an intrinsic dynamic phenomenon. The intrinsic dynamics of allosteric proteins are defined by their topology of inter-residue contacts and favor cooperative motions that are plausibly structural changes approximated to their allosteric and binding actions. Moreover, the structure of Rac1-PAK1 complex has not been experimentally determined yet, so we try to enlighten the mutation-driven changes in binding interfaces of Rac1 through analyzing intrinsic dynamic events. We quest here the structural and dynamic response of Rac1 to the active mutations. To this, extensive MD simulations have been performed on the GTP-bound wt, Q61L, Y72C, P29S and Q61R, and GTP-free T17N Rac1s. Except the dominant-negative T17 mutant, Rac1s do not undergo significant conformational changes but display subtle dynamical changes (Figure S5), as will be described below.

Mutations modify the allosteric communication among binding interfaces of Rac1

Rac1 acts through its interactions with GTP/Mg^{2+}, upstream proteins (GEF, GDI and GAP) and downstream partner PAK1. The active mutations affect the global dynamics of Rac1 underlying the cooperativity of allosteric binding interactions with the change in the local interactions and hydrogen bonding and residue conformational preferences particularly at critical binding residues with Mg^{2+}/GTP and upstream/downstream partners, as presented below.

Rac1's interactions with Mg^{2+} ion and GTP. The active mutations, except Y72C, allosterically changes the position of Mg^{2+} and the stability of GTP with redistribution of hydrogen bonds around GTP (Figures 4, S6(A-B), S7 and S8).

The nucleotide controls the positioning of switch loops through binding to the pocket between p-loop (G10-T17), Switch I (F28, Y32, P34, T35), Switch II (Q60), Helix 6 (K116, D118 and L119) and residues S158-L160 (3) (Figure 2B). T17, T35 and D57 of Rac1 in coordination with Mg^{2+}, are critical for the activation cycle of Rac1. While the distances of Mg^{2+} to these three residues display a unimodal distribution for wt Rac1, multimodal distances observed in mutant Rac1s display the change in the relative proximity of Mg^{2+} with GTP and Rac1 and also the change in H-bonding. We observe that H-bond occupancy of T17 (main) and T35 (side) with GTP decreases with compensating new H-bonds between K16 (side) and S29 (main) and GTP in P29S Rac1 (Figure 4). This new S29-GTP H-bond observed in P29S Rac1 was previously shown to alter the structure into a Ras-like Switch I conformation with increased effector activation (20). Likewise, Q61L and Q61R Rac1s, especially for Q61L, also show a significant decrease in H-bond occupancies of T17 (main) and T35 (side) with GTP (Figure 4). However, Q61R gains a new compensating H-bond between R61 and GTP, reflecting a distinct behavior between two different mutations of the same position. We speculate that these phenomenal changes in H-bonding with interatomic distances around GTP-binding and Mg^{2+} coordinating residues alter the coordination of the nucleotide in a non-hydrolyzable manner in the constitutively active Q61L, whereas Q61R Rac1 can withstand this effect and still stabilize the nucleotide in a hydrolyzable state with the help of the newly gained H-bond. On the other hand, although D57 approaches both GTP and Mg^{2+} significantly, it does not form a H-bond with GTP, instead it forms a new H-bond with GTP-binding and Mg^{2+}-coordinating residue T35 in the proximity of PAK1-binding interface only in Q61L Rac1. Y72C Rac1 behaves similar to wt Rac1 in terms of residue distances to Mg^{2+}/GTP and H-bonds with GTP.

Together with distances and H-bonding, the side chain dihedral angles of Mg^{2+}-coordinating and GTP-binding T17 and T35 also show distinctive characteristics (Figure S10). The median values of Chi1 angle residues T17 and T35 shift with all mutations, except Y72C, and most significantly with T17N Rac1 (Figure S10), implying higher variation/flexibility of these residues with altered orientations and explaining the loss of H-bonds with GTP around this region with all of the active mutations except Y72C. Moreover, T35 has two states in Q61L Rac1 and three states in P29S Rac1 (Figure S10). In parallel, we observe a higher flexibility of Y32 and T35 in P29S, Q61L and Q61R Rac1s, whereas T35 is slightly more restricted in Y72C Rac1.

Change in mechanics at the upstream/downstream binding partners. Rac1's upstream and downstream binding partners as well GTP share some of the same Rac1's residues in their interactions. V36 and F37 on Switch I and D63, Y64 and L67 on Switch II, being also PAK1-binding sites, are seen as the predominant contacts with GAP on Rho family GTPases (7) (Figure 2B). Moreover, the mutation of D38 and N39 on Switch I and Q61, Y64, R66 and L67 on Switch II lead to loss of GEF binding indicating their involvement is GEF binding (55). Also, W56 is crucial for the recognition by GEFs, and Y32, D65, L70 and S71 are important in the catalysis of efficient exchange of nucleotides (GDP-to-GTP) during activation (55). On the other hand, T35, V36, Y64, R66, L67, L70, P73, H103 and H104, as based on Cdc42, were suggested as GDI-interacting residues (31).

Flexibility at a given region of a protein structure is reflected by its range of fluctuations in the backbone and/or side dihedral angles. The difference of backbone dihedral angle mean square fluctuations of each mutant with respect to wt is given in Figure S11. The main difference in the backbone flexibility is observed mainly at switch regions, which comprise the binding interfaces of both GTP and upstream/downstream partners including PAK1-binding interfaces.

PAK1, GEF, GDI and GAP can competitively bind to Rac1 using shared interface residues such as V36-N39 on Switch I and Q61, N63, Y64, R66 and L67 on Switch II. Among common binding residues, the most profound difference is observed in the side chain conformations of V36 and F37 (Figure S12). The Chi1 (first side chain dihedral angle) angle of PAK1- and GAP-binding V36 cluster into two orientations in wt and P29S Rac1 whereas only one of these orientations are sampled in Y72C and Q61L Rac1 which is rarely sampled in Q61R and T17N Rac1. (Figures S12, Table S3). The NMR structure of Cdc42 in complex with PAK1 (PDB ID: 1e0a) significantly samples the same orientation as Y72C and Q61L. F37 has a single state, which is the only sampled state of Cdc42 in complex with PAK1, with a very low variability in wt and Y72C Rac1s (Figure S12 and Table S3). The

backbone flexibility reflected by the fluctuations of backbone angles of these two residues supports the importance of these sites in competitive upstream/downstream binding (Figure S13). The flexibility of V36 and F37 are significantly higher in the P29S Rac1, whereas they are slightly more rigid in Q61L and Y72C compared to wt. Knowing that Q61L is unfavorable for GAP binding and the mutant has a defect in the GTP hydrolysis function, we can deduce that V36 and F37 rigidify and the side chains sample a position more suitable for PAK1-binding with Q61L and Y72C and for GAP-binding with Q61R mutation.

Among the PAK1 only binding interface, the most profound increase in backbone flexibility is observed in residues T25, N26, Y32, P34, M45, V46, A59, G60, D63 and Y64 in all mutants compared to wt (see Figure S14). T25 and N26 have higher flexibility in Y72C and T17N Rac1 and relatively subtle increase is observed in P29S compared to wt whereas no change is observed in case of Q61L/R. For T17N Rac1, increased flexibility is expected as these residues are in the vicinity of nucleotide binding pocket but for Y72C mutation, this change is an allosteric effect of oncogenic mutation. On the other hand, I33, P34, M45 and V46 have higher flexibility in Q61L, P29S and T17N compared to wt, Y72C, Q61R Rac1. Increased flexibility in these regions indicates a mechanically softer binding interface. This result agrees with the longer distance to the transition state obtained from SMFS experiments for Q61L and Y72C mutants compared to wt.

GTP-independent intrinsic dynamics of Rac1. The dominant negative T17N mutant, which has no bound nucleotide, behaves similar to the active mutants (even more intensified) in terms of cooperativity with respect to wt Rac1 (Figure 5). Moreover, for almost all residues, the nucleotide free T17N mutant Rac1 spans a wider backbone conformational space, having the highest degree of flexibility with respect to wt and active mutant Rac1s and interestingly encapsulates the conformational variation of the mutant Rac1s (Figures S11). The tendency of the nucleotide free form to approach the GTP-bound states in terms of free energy surfaces was also demonstrated for RhoGTPases previously (56). Thus, it can be concluded that activating mutations can affect the dynamics of Rac1 in a GTP-independent intrinsic manner.

Changes in fluctuations and cooperativity. Significant changes in the occupancy of H bonds and the inter-atomic distances in the vicinity of the nucleotide-binding pocket affect the positional fluctuations of GTP (Figures S7-S9, see details in SI) with mutations. T17N Rac1 shows the highest residue fluctuations overall but especially around GTP-binding residues, due to the lack of a bound nucleotide (Figure S15). Higher residue fluctuations of GTP are also observed in the binding cavity of P29S, Q61L and Q61R Rac1s (Figure S6B). While Switch I in P29S and Q61L displaying the highest fluctuations, Switch II in Y72C display the most significant restriction in its fluctuations (Figure S15). Specifically, the Y32-T35 region on Switch I that is crucial in nucleotide stabilization is fairly immobile in wt and Y72C Rac1s. This region gets more mobile with P29S and Q61R and gains the highest mobility in Q61L (around an RMSF value of 1.5Å) (Figure S15).

GTP-binding residues within wt Rac1 are inter-correlated such that the nucleotide binding p-loop (G10-T17) and α1 region (G15-T25) are strongly correlated with mainly three other regions containing the GTP-binding residues: the beginning of Switch I (GTP-binding residues F28, Y32, P34, T35); K116, D118, L119 region and S158-L160 region (Figure 5B, see wt in GTP_1 vs. GTP_2 and PAK1_1 vs. GTP_2 regions). The α1 region partially contains PAK1-binding residues (L20, I21, Y23-T25 between p-loop and Switch I, so GTP- and PAK1-binding residues are also cooperative in wt Rac1. The mutants show a commonality in the behavior of correlation changes with respect to wt Rac1, but some changes being more prominent in certain regions for different mutants. When the correlation differences from wt Rac1 are considered, it is immediately observed that p-loop and α1 PAK1-binding residues (named as GTP_1 And PAK1_1, respectively in Figure 5) lose cooperativity with the other GTP-binding regions (GTP_2 in Figure 5) in all mutations, most significantly with Q61L and T17N (Figure 5A&B, GTP_1 vs. GTP_2 and GTP_2_2&2_3 vs. PAK_1_1 regions).

On the other hand, some of the GTP-binding residues are not correlated with some PAK1-binding residues and some PAK1-binding regions are not correlated with each other in wt Rac1 (Figure 5B, see wt in box plots for GTP_2_2&GTP_2_3 vs. PAK1_3; GTP_2_1 vs. PAK1_3; PAK1_1 vs. PAK1_4 and PAK1_1 vs. PAK1_4 regions) but show increased correlations with certain mutations (see P29S, Q61L and Y72C in respective plots in Figure 5B and maps in Figure 5A). Q61L also has increased correlations of GTP-binding residues with PAK1-binding residues at the end of Switch II (R66, L67, L70), including the critical PAK1-, GEF-, GDI- and GAP-binding residue L67 (Figure 5A&B,

GTP_2_2&2_3 vs. PAK_1_3 region). One of the most remarkable and unique changes with Y72C mutation is the increase in cooperativity around Switch II PAK1-, GEF-, GDI- and GAP-binding residue L67 and Switch I GTP-binding residue T35 (Figure 5A&B, GTP_2_1 vs. PAK1_3 region).

Binding energies of modeled Rac1-Pak1 complexes from representative MD sampled conformations. MD sampled conformations are clustered to disclose if there are distinctly behaving conformational ensembles by wt and mutant Rac1s. wt Rac1 forms two main relatively evenly populated ensembles. The mutants, however, show either a single cluster (Y72C and Q61R) or multiple clusters with a major one comprising about 70% of the population (P29S and Q61L) (Table 2 and Figure S17). Moreover, the dominant negative T17N Rac1, without a bound nucleotide, has six clusters with one dominating conformational state. Within the time window of MD simulations, we observe a shift in the conformational space with the mutations such that the correlated residue motions of the mutants with respect to wt Rac1, reveal significant changes especially around the GTP-binding residues that are similar to the correlation differences of two clusters of wt Rac1 (Figure 5). Rac1-GTP H-bonding occupancies of different clusters are also subject to changes with mutations that vary among different clusters of mutations (Figure S18).

The representatives of wt and mutant Rac1 clusters are then used to model Rac1-PAK1 complexes and predict plausible effects of the mutations on the binding behavior based on their predicted binding energy and free energy of dissociation (see Table 2). The predicted binding energies of the modeled complex structures are estimated by the global binding energy calculated at the end of the flexible refinement step of PRISM algorithm (57, 58) by employing FiberDock (flexible induced-fit backbone refinement in molecular docking) (59). FiberDock scores and ranks the putative complexes by including a variety of energy terms, such as desolvation (atomic contact) energy, vdW interactions, partial electrostatics, hydrogen and disulfide bonds, π-stacking and aliphatic interactions. Moreover, the free energy of assembly dissociation ΔG^{diss} (in kcal/mol) values of the modeled complex structures are predicted by PDBePISA (Proteins, Interfaces, Structures and Assemblies) server (60). The average predicted binding energies of the two most populated wt Rac1 clusters are -104 (Cluster 2–with 53%) and -93 (Cluster 3–with 38%) with the corresponding average free energy of dissociation values 6.5 and 5.7 kcal/mol (Tables 2, S2 and Figure S17; the details of clustering Rac1s and modeling Rac1-PAK1 complex structures are discussed in SI).

The consistent binding behavior with lower binding energy (stronger binding) and higher energy of dissociation (more difficult dissociation) as well as the mutant Rac1s assuming mainly the cooperative behavior of one of the clusters of wild-type Rac1 along with SMFS observations permit us to map the correspondence between the two most populated clusters (cluster2 and cluster3) of the MD simulations and two proposed states; the state 1 and state 2, from AFM experiments in wt Rac1, respectively. This is also shown in a recent work (56), in which GTP-bound RhoGTPases were observed to have intermediate states and constitutively active G14V mutant RhoA (G12V in Rac1) was observed to shift the protein towards a state in which Switch I has increased flexibility that may result in the promotion of arbitrary effector binding through induced fit and hence activation of downstream effectors in a less selective/specific manner (56).

Conclusion

The GNM analyses with MD simulations show the deformation of global modes of motion with the functional mutations, namely; dominant-negative T17N, constitutively active Q61L, oncogenic P29S and Q61R, and Y72C. This deformation modifies Rac1's intrinsic dynamics and affects binding interactions with GTP, PAK1, GEF and GAP.

In the specific case of PAK1, Q61L and Y72C mutations in Rac1 display a shift in the dynamic ensemble as such to favor PAK1-binding in interaction with altered GTP-binding behavior, as supported by AFM-based SMFS experiments. The unbinding behavior of Rac1-PAK1 complex reveals the existence of at least two dynamic states, state 1 and state 2, of wt Rac1-PAK1, which is reduced to a single state with Q61L and Y72C mutations. A decrease in the dissociation rate similar to state 1 yet similar unbinding forces with respect to state 2 of wt Rac1 implies a shift of the dynamic state towards a more stable Rac1-PAK1 complex with the active mutations. The active Q61L and oncogenic Y72C mutations also alter the mechanics of the molecule(s). The distance to the transition state in the unbinding energy landscape increases. So, the elasticity of the protein increases, resulting in a slower

transition to the unbound state. The change in mechanics is more drastic in Y72C than Q61L. This demonstrates that active mutations, especially oncogenic ones, alter the mechanics of Rac1 and affect its interactions with other molecules. Change in mechanical properties is supported by the results obtained from extensive atomistic MD simulations. Analyses of the backbone and side chain angle rotation, together with H-bonding network and correlated motions within and among GTP- and PAK1-binding interfaces reveal more flexible GTP- and PAK1-binding residues on Switch I and Switch II with Q61L and Y72C as well as oncogenic P29S and Q61R and negative T17N. The predicted binding free energies of the modeled Rac1-PAK1 complexes indicate a more favorable PAK1 interaction. Our concerted results suggest that the active mutations affect intrinsic functional dynamic events, and alter the mechanics underlying the binding of Rac1 to GTP and upstream/downstream partners including PAK1.

In conclusion, although the positions of the mutations appear seemingly sporadic, they have commonality of aligning with the global hinges and have the dynamic capacity to affect the natural functional cycle of Rac1. Thus, in response to any perturbations to Rac1's intrinsic dynamics, both upstream and downstream interactions are affected due to an allosterically regulated interplay between the functionally important regions on Rac1, leading to the activation of cell signaling networks.

Author Contributions

SEA and FS performed computational and experimental research and contributed equally to this work. SEA, FS, HT and TH designed research, analyzed data and wrote the paper.

Acknowledgments

The financial support of Scientific and Technological Research Council of Turkey (TUBITAK, grant no. 112T569) is gratefully acknowledged. We thank Dr. Hyunbum Jang for his assistance with topology and parameter file for GTP, used in the MD simulations, and Prof. Dr. Ruth Nussinov for our fruitful discussions. We also thank Büşra Özgüney for her contribution in Figure S2.

References

1. Jaffe, A. B., and A. Hall. 2005. Rho GTPases: biochemistry and biology. Annual review of cell and developmental biology 21:247-269.
2. Ridley, A. J., H. F. Paterson, C. L. Johnston, D. Diekmann, and A. Hall. 1992. The small GTP-binding protein rac regulates growth factor-induced membrane ruffling. Cell 70(3):401-410.
3. Vetter, I. R., and A. Wittinghofer. 2001. The guanine nucleotide-binding switch in three dimensions. Science 294(5545):1299-1304.
4. Davis, M. J., B. H. Ha, E. C. Holman, R. Halaban, J. Schlessinger, and T. J. Boggon. 2013. RAC1P29S is a spontaneously activating cancer-associated GTPase. Proceedings of the National Academy of Sciences of the United States of America 110(3):912-917.
5. Bos, J. L., H. Rehmann, and A. Wittinghofer. 2007. GEFs and GAPs: critical elements in the control of small G proteins. Cell 129(5):865-877.
6. Moon, S. Y., and Y. Zheng. 2003. Rho GTPase-activating proteins in cell regulation. Trends in cell biology 13(1):13-22.
7. Owen, D., and H. R. Mott. 2005. Structural Analysis of Rho Protein Complexes, in: Rho Family GTPases. Springer Netherlands.
8. Sasaki, T., M. Kato, and Y. Takai. 1993. Consequences of weak interaction of rho GDI with the GTP-bound forms of rho p21 and rac p21. The Journal of biological chemistry 268(32):23959-23963.
9. Manser, E., T. Leung, H. Salihuddin, Z. S. Zhao, and L. Lim. 1994. A brain serine/threonine protein kinase activated by Cdc42 and Rac1. Nature 367(6458):40-46.
10. Bokoch, G. M. 2003. Biology of the p21-activated kinases. Annual review of biochemistry 72:743-781.
11. Price, L. S., and J. G. Collard. 2001. Regulation of the cytoskeleton by Rho-family GTPases: implications for tumour cell invasion. Seminars in cancer biology 11(2):167-173.
12. Schmitz, A. A., E. E. Govek, B. Bottner, and L. Van Aelst. 2000. Rho GTPases: signaling, migration, and invasion. Experimental cell research 261(1):1-12.
13. Chan, A. Y., S. J. Coniglio, Y. Y. Chuang, D. Michaelson, U. G. Knaus, M. R. Philips, and M. Symons. 2005. Roles of the Rac1 and Rac3 GTPases in human tumor cell invasion. Oncogene 24(53):7821-7829.
14. Espina, C., M. V. Cespedes, M. A. Garcia-Cabezas, M. T. Gomez del Pulgar, A. Boluda, L. G. Oroz, S. A. Benitah, P. Cejas, M. Nistal, R. Mangues, and J. C. Lacal. 2008. A critical role for Rac1 in tumor progression of human colorectal adenocarcinoma cells. The American journal of pathology 172(1):156-166.
15. Niggli, V., D. Schlicht, and S. Affentranger. 2009. Specific roles of Rac1 and Rac2 in motile functions of HT1080 fibrosarcoma cells. Biochemical and biophysical research communications 386(4):688-692.
16. Vega, F. M., and A. J. Ridley. 2008. Rho GTPases in cancer cell biology. FEBS letters 582(14):2093-2101.
17. Ellenbroek, S. I., and J. G. Collard. 2007. Rho GTPases: functions and association with cancer. Clinical & experimental metastasis 24(8):657-672.
18. Alan, J. K., and E. A. Lundquist. 2013. Mutationally activated Rho GTPases in cancer. Small GTPases 4(3):159-163.
19. Porter, A. P., A. Papaioannou, and A. Malliri. 2016. Deregulation of Rho GTPases in cancer. Small GTPases 7(3):123-138.
20. Krauthammer, M., Y. Kong, B. H. Ha, P. Evans, A. Bacchiocchi, J. P. McCusker, E. Cheng, M. J. Davis, G. Goh, M. Choi, S. Ariyan, D. Narayan, K. Dutton-Regester, A. Capatana, E. C. Holman, M. Bosenberg, M. Sznol, H. M. Kluger, D. E. Brash, D. F. Stern, M. A. Materin, R. S. Lo, S. Mane, S. Ma, K. K. Kidd, N. K. Hayward, R. P. Lifton, J. Schlessinger, T. J. Boggon, and R. Halaban. 2012. Exome sequencing identifies recurrent somatic RAC1 mutations in melanoma. Nature genetics 44(9):1006-1014.
21. Hodis, E., I. R. Watson, G. V. Kryukov, S. T. Arold, M. Imielinski, J. P. Theurillat, E. Nickerson, D. Auclair, L. Li, C. Place, D. Dicara, A. H. Ramos, M. S. Lawrence, K. Cibulskis, A. Sivachenko, D. Voet, G. Saksena, N. Stransky, R. C. Onofrio, W. Winckler, K. Ardlie, N. Wagle, J. Wargo, K. Chong, D. L. Morton, K. Stemke-Hale, G. Chen, M. Noble, M. Meyerson, J. E. Ladbury, M. A. Davies, J. E. Gershenwald, S. N. Wagner, D. S. Hoon, D. Schadendorf, E. S. Lander, S. B. Gabriel, G. Getz, L. A. Garraway, and L. Chin. 2012. A landscape of driver mutations in melanoma. Cell 150(2):251-263.

22. Machesky, L. M., and O. J. Sansom. 2012. Rac1 in the driver's seat for melanoma. Pigment cell & melanoma research 25(6):762-764.
23. Forbes, S. A., G. Bhamra, S. Bamford, E. Dawson, C. Kok, J. Clements, A. Menzies, J. W. Teague, P. A. Futreal, and M. R. Stratton. 2008. The Catalogue of Somatic Mutations in Cancer (COSMIC). Current protocols in human genetics / editorial board, Jonathan L. Haines ... [et al.] Chapter 10:Unit 10 11.
24. Gao, J., B. A. Aksoy, U. Dogrusoz, G. Dresdner, B. Gross, S. O. Sumer, Y. Sun, A. Jacobsen, R. Sinha, E. Larsson, E. Cerami, C. Sander, and N. Schultz. 2013. Integrative analysis of complex cancer genomics and clinical profiles using the cBioPortal. Science signaling 6(269):pl1.
25. Cerami, E., J. Gao, U. Dogrusoz, B. E. Gross, S. O. Sumer, B. A. Aksoy, A. Jacobsen, C. J. Byrne, M. L. Heuer, E. Larsson, Y. Antipin, B. Reva, A. P. Goldberg, C. Sander, and N. Schultz. 2012. The cBio cancer genomics portal: an open platform for exploring multidimensional cancer genomics data. Cancer discovery 2(5):401-404.
26. Chang, M. T., S. Asthana, S. P. Gao, B. H. Lee, J. S. Chapman, C. Kandoth, J. Gao, N. D. Socci, D. B. Solit, A. B. Olshen, N. Schultz, and B. S. Taylor. 2016. Identifying recurrent mutations in cancer reveals widespread lineage diversity and mutational specificity. Nature biotechnology 34(2):155-163.
27. Karnoub, A. E., and C. J. Der. 2003. Rho family GTPases and cellular transformation. In: Marc Symons (ed) Signal Transduction: Rho-GTPases. Landes Biosciences Pub. Co.
28. Smithers, C. C., and M. Overduin. 2016. Structural Mechanisms and Drug Discovery Prospects of Rho GTPases. Cells 5(2).
29. Wu, W. J., R. Lin, R. A. Cerione, and D. Manor. 1998. Transformation activity of Cdc42 requires a region unique to Rho-related proteins. The Journal of biological chemistry 273(27):16655-16658.
30. Schaefer, A., N. R. Reinhard, and P. L. Hordijk. 2014. Toward understanding RhoGTPase specificity: structure, function and local activation. Small GTPases 5(2):6.
31. Hoffman, G. R., N. Nassar, and R. A. Cerione. 2000. Structure of the Rho family GTP-binding protein Cdc42 in complex with the multifunctional regulator RhoGDI. Cell 100(3):345-356.
32. Cherfils, J., and M. Zeghouf. 2013. Regulation of small GTPases by GEFs, GAPs, and GDIs. Physiological reviews 93(1):269-309.
33. Kumar, A., V. Rajendran, R. Sethumadhavan, and R. Purohit. 2013. Molecular dynamic simulation reveals damaging impact of RAC1 F28L mutation in the switch I region. PloS one 8(10):e77453.
34. Hall, A., and A. J. Self. 1986. The effect of Mg2+ on the guanine nucleotide exchange rate of p21N-ras. The Journal of biological chemistry 261(24):10963-10965.
35. Zhang, B., Y. Zhang, Z. Wang, and Y. Zheng. 2000. The role of Mg2+ cofactor in the guanine nucleotide exchange and GTP hydrolysis reactions of Rho family GTP-binding proteins. The Journal of biological chemistry 275(33):25299-25307.
36. Morreale, A., M. Venkatesan, H. R. Mott, D. Owen, D. Nietlispach, P. N. Lowe, and E. D. Laue. 2000. Structure of Cdc42 bound to the GTPase binding domain of PAK. Nature structural biology 7(5):384-388.
37. Rajendran, V., C. Gopalakrishnan, and R. Purohit. 2016. Impact of point mutation P29S in RAC1 on tumorigenesis. Tumour biology : the journal of the International Society for Oncodevelopmental Biology and Medicine 37(11):15293-15304.
38. Lu, S., H. Jang, R. Nussinov, and J. Zhang. 2016. The Structural Basis of Oncogenic Mutations G12, G13 and Q61 in Small GTPase K-Ras4B. Scientific reports 6:21949.
39. Grant, B. J., A. A. Gorfe, and J. A. McCammon. 2009. Ras conformational switching: simulating nucleotide-dependent conformational transitions with accelerated molecular dynamics. PLoS computational biology 5(3):e1000325.
40. Chen, J., W. Wang, L. Pang, and W. Zhu. 2020. Unveiling conformational dynamics changes of H-Ras induced by mutations based on accelerated molecular dynamics. Physical chemistry chemical physics : PCCP 22(37):21238-21250.
41. Ridley, A. 2000. Rho GTPases. Integrating integrin signaling. The Journal of cell biology 150(4):F107-109.
42. De, P., J. C. Aske, and N. Dey. 2019. RAC1 Takes the Lead in Solid Tumors. Cells 8(5).
43. Zhang, Y., P. Doruker, B. Kaynak, S. Zhang, J. Krieger, H. Li, and I. Bahar. 2020. Intrinsic dynamics is evolutionarily optimized to enable allosteric behavior. Current opinion in structural biology 62:14-21.

44. Haliloglu, T., and I. Bahar. 2015. Adaptability of protein structures to enable functional interactions and evolutionary implications. Current opinion in structural biology 35:17-23.
45. Emekli, U., D. Schneidman-Duhovny, H. J. Wolfson, R. Nussinov, and T. Haliloglu. 2008. HingeProt: automated prediction of hinges in protein structures. Proteins 70(4):1219-1227.
46. Sumbul, F., S. E. Acuner-Ozbabacan, and T. Haliloglu. 2015. Allosteric Dynamic Control of Binding. Biophysical journal 109(6):1190-1201.
47. Bahar, I., and R. L. Jernigan. 1998. Vibrational dynamics of transfer RNAs: comparison of the free and synthetase-bound forms. Journal of molecular biology 281(5):871-884.
48. Haliloglu, T., I. Bahar, and B. Erman. 1997. Gaussian dynamics of folded proteins. Physical Review Letters 79:3090.
49. Sayilgan, J. F., T. Haliloglu, and M. Gonen. 2019. Protein dynamics analysis reveals that missense mutations in cancer-related genes appear frequently on hinge-neighboring residues. Proteins 87(6):512-519.
50. Ozen, A., M. Gonen, E. Alpaydin, and T. Haliloglu. 2009. Machine learning integration for predicting the effect of single amino acid substitutions on protein stability. Bmc Struct Biol 9.
51. Marszalek, P. E., H. Lu, H. Li, M. Carrion-Vazquez, A. F. Oberhauser, K. Schulten, and J. M. Fernandez. 1999. Mechanical unfolding intermediates in titin modules. Nature 402(6757):100-103.
52. Evans, E., and K. Ritchie. 1997. Dynamic strength of molecular adhesion bonds. Biophysical journal 72(4):1541-1555.
53. Bell, G. I. 1978. Models for the specific adhesion of cells to cells. Science 200(4342):618-627.
54. Schwesinger, F., R. Ros, T. Strunz, D. Anselmetti, H. J. Guntherodt, A. Honegger, L. Jermutus, L. Tiefenauer, and A. Pluckthun. 2000. Unbinding forces of single antibody-antigen complexes correlate with their thermal dissociation rates. Proceedings of the National Academy of Sciences of the United States of America 97(18):9972-9977.
55. Gao, Y., J. Xing, M. Streuli, T. L. Leto, and Y. Zheng. 2001. Trp(56) of rac1 specifies interaction with a subset of guanine nucleotide exchange factors. The Journal of biological chemistry 276(50):47530-47541.
56. Kumawat, A., S. Chakrabarty, and K. Kulkarni. 2017. Nucleotide Dependent Switching in Rho GTPase: Conformational Heterogeneity and Competing Molecular Interactions. Scientific reports 7:45829.
57. Tuncbag, N., A. Gursoy, R. Nussinov, and O. Keskin. 2011. Predicting protein-protein interactions on a proteome scale by matching evolutionary and structural similarities at interfaces using PRISM. Nature protocols 6(9):1341-1354.
58. Baspinar, A., E. Cukuroglu, R. Nussinov, O. Keskin, and A. Gursoy. 2014. PRISM: a web server and repository for prediction of protein-protein interactions and modeling their 3D complexes. Nucleic acids research 42(Web Server issue):W285-289.
59. Mashiach, E., R. Nussinov, and H. J. Wolfson. 2010. FiberDock: a web server for flexible induced-fit backbone refinement in molecular docking. Nucleic acids research 38(Web Server issue):W457-461.
60. Krissinel, E., and K. Henrick. 2007. Inference of macromolecular assemblies from crystalline state. Journal of molecular biology 372(3):774-797.

Tables

Table 1. Energy Landscape Parameters.

Ligand-Receptor		**Loading rate range (pN/s)**	**x_β (nm)**	**k_{off} (s^{-1})**	**ΔΔE (k_BT)***	
Wild-type Rac1-PAK1	State 2	3.5×10^{2}-1.4×10^{4}	0,22	5,5		
		1.4×10^{4}-1.7×10^{5}	0,06	46,2		
	State 1	1.6×10^{3}-6.2×10^{4}	0,12	0,2		
Q61L Rac1-PAK1		3.2×10^{2}-2.1×10^{4}	0,44	1,2	1,5	
		2.1×10^{4}-6.5×10^{4}	0,05	121,0	-1,0	
Y72C Rac1-PAK1		1.6×10^{2}-7.1×10^{4}	0,47	0,5	2,4	0,9
		7.1×10^{4}-9.6×10^{4}	0,15	28,5	0,5	1,4
* ΔΔE is relative to wild-type Rac1-PAK1 binding energy						

Table 2. Ensembles of Rac1 conformations and binding properties of the modeled Rac1 (cluster averages)-PAK1 complexes.

Structure_cluster#	Member % in the cluster	Parallel MD runs represented in the cluster	Average Global Binding Energy of the top ten cluster members (FiberDock, unitless (59))	Average ΔG^{diss} of the top ten cluster members (PDBePISA, kcal/mol (60))
wild-type_cluster 2 (State 1)	53.3	1-2-3-4	-104	6.5
wild-type_cluster 3 (State 2)	38.2	1-2-3-4	-93	5.7
Y72C_cluster 1	100	1-2-3-4	-91	5.9
Q61R_cluster 1	100	1-2-3-4	-96	5.9
Q61L_cluster 1	67.6	1-3-4	-106	5.5
Q61L_cluster 2	17	2	-86	6.8
P29S_cluster 1 (State 1)	70.7	1-2-3	-97	5.6
P29S_cluster 2 (State 2)	25	4	-82	3.8
T17N_cluster1	60	1-2-3	-51	3.1

Figure Legends

Figure 1. Rac1 activation/deactivation cycle.

Figure 2. Dynamic and functional domains and oncogenic mutations on Rac1. (A) Functional domains: p-loop (orange: res. 10-17, GTP-binding), Switch I (magenta: res. 26-45, downstream effector), Switch II (yellow: res. 59-74, activation loop), Insert (cyan: res. 124-135) regions shown as spheres on the cartoon representations of Rac1 structure. (B) GTP-binding residues (orange: res. 10-17, 28, 32, 34, 35, 60, 116, 118, 119, 158-160) and PAK1-binding residues (magenta: res. 20, 21, 23-25, 27, 31, 33, 34, 36-47, 56, 58, 63, 64, 66, 67, 70, 165, 166, 169, 170, 173, 174. Rac1-PAK1 binding interface was extracted from Cdc42-PAK1 and Rac3-PAK1 complex structures (PDB IDs: 1e0a and 2qme) using HotRegion server (http://prism.ccbb.ku.edu.tr/hotregion/)). Common with PAK1-binding are some GAP-binding (yellow: res. 36, 37, 63) and GEF-binding (blue: res. 38, 39, 61, 66) and both GEF and GAP-binding regions (cyan: 64, 67) shown as spheres. (C) All oncogenic mutations corresponding (white spheres) and not corresponding (orange spheres) to first three slowest modes and the selected case study mutations T17, P29, Q61 and Y72 (red spheres). (D-F) Dynamic domains of Rac1 of first three slowest modes of motion: Red and blue display two dynamic domains moving in opposite directions and green regions are hinge sites. The oncogenic mutations are shown in yellow close to/on the hinge sites (spheres are on the hinges and lines are nearby residues).

Figure 3. The design of AFM pulling experiments. (A) Schematic representation of Rac1-PAK1 experiment setup. (B) Example experimental force-distance traces of low (top) and high (bottom) unbinding forces for wt Rac1-PAK1 complex at 1 μm/s pulling velocity. Calculation of loading rate and rupture force are indicated on the exemplary curve. The polymeric extension profile of the curves is due to the stretching of the PEG linker. (C) The probability of adhesion of wild-type, T17N, Q61L and Y72C Rac1- PAK1 observed during experiments. (D) Most probable rupture forces of wild-type Rac1-PAK1 complex depending on the loading rates are shown with triangle data points for the state 1 and square data points for state 2 with the SEMs and the fitted linear relation is shown with straight and dashed lines, respectively. Two distinct linear regimes describe the best relation for the state 2 corresponding to the two distinct activation energy barrier of the dissociation reaction of the complex. (E) Rupture force spectra of Q61L Rac1-PAK1 complex shown in square data points with the SEMs and the fitted linear relation is shown with straight line. Two distinct linear regimes fitted to the relation corresponding to the two distinct activation energy barriers of the complex dissociation reaction. (F) Rupture force spectra of Y72C Rac1-PAK1 complex. shown in square data points with the SEMs and the fitted linear relation is shown with straight line. Two distinct linear regimes fitted to the relation corresponding to the two distinct activation energy barriers of the complex dissociation reaction.

Figure 4. Box plot of H-bonding occupancies between Rac1 and GTP at different systems. The red line is the median; the boxes show the 25th and 75th percentiles, and whiskers represent 2.7-times the standard deviation. The H-bonds with an occupancy higher than 20% are considered. There is a significant decrease in the occupancies of H-bonds between GTP-T17 and GTP-T35 with P29S, Q61L and Q61R. The H-bond between GTP-Y32 also decreases upon Q61L and diminishes with Q61R, whereas GTP-K16(main) also diminishes upon Q61L/R mutations. The occupancy of H-bond between GTP-K16 increases and a new H-bond is formed between GTP-R61 with Q61R. Similarly, the occupancy of H-bond between GTP-K16 (main and side) increases and a new H-bond is formed between GTP-S29 with P29S.

Figure 5. Correlation differences of mutants from wild-type Rac1 and the differences between the two wild-type clusters. (A) On correlation difference maps, Rac1 structures are colored by average correlations for GTP-binding residues 28, 32, 34, 35, 60, 116, 118, 119, 158-160. The residues corresponding to the regions on x-axis are listed below. GTP_1 (p-loop): res. 10-17; GTP_2 is composed of 3 sub-regions as GTP_2_1: res. 28, 32, 34, 35; GTP_2_2: res. 116, 118, 119 and GTP_2_3: res. 158, 159, 160; PAK1_1: res. 20, 21, 23, 24, 25; PAK1_2: res. 41-45; PAK1_3: 66, 67, 70 and PAK1_4: 169, 170, 173, 174. Transparent spheres on the bottom of the structures represent PAK1 structure taken from PDB ID 1e0a. The encircled regions show significant differences in the mutants with respect to wt Rac1, when all the parallel runs are considered. (B) Box plot of Rac1's mean cross correlations coming from parallel runs for different regions at different systems. The red line is the median; the boxes show the 25th and 75th percentiles, and whiskers represent 2.7-times the standard deviation.

Figure 1:

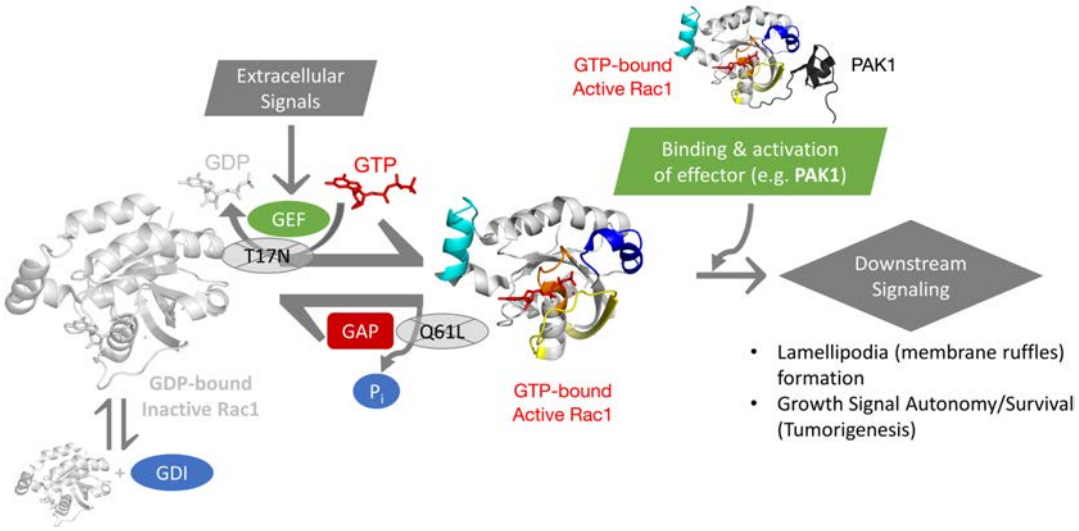
Extracellular Signals
GDP
GTP
GEF
T17N
GAP
Q61L
P_i
GDP-bound Inactive Rac1
GDI
GTP-bound Active Rac1
GTP-bound Active Rac1
PAK1
Binding & activation of effector (e.g. PAK1)
Downstream Signaling
• Lamellipodia (membrane ruffles) formation
• Growth Signal Autonomy/Survival (Tumorigenesis)

Figure 2:

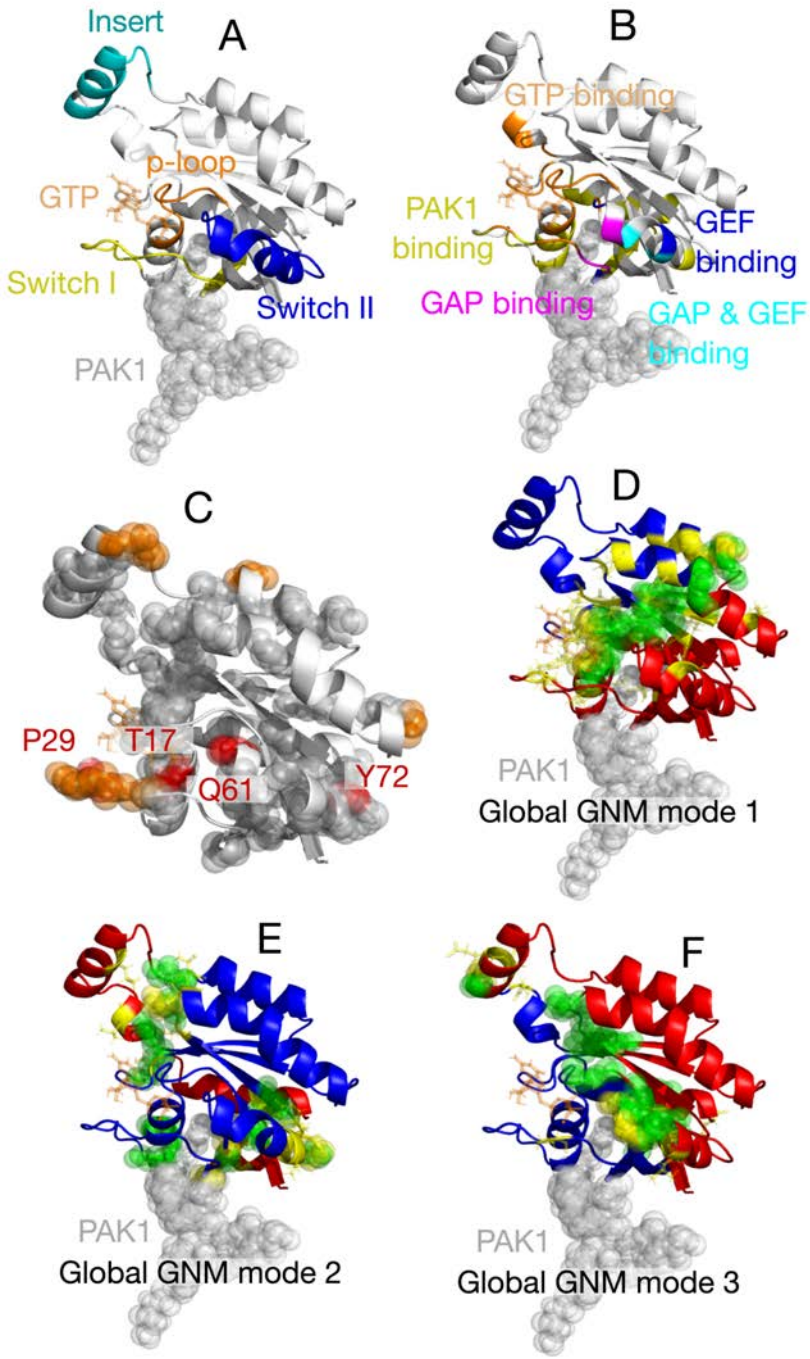
A
Insert
p-loop
GTP
Switch I
Switch II
PAK1
B
GTP binding
PAK1
binding
GEF
binding
GAP binding
GAP & GEF
binding
C
P29
T17
Q61
Y72
D
PAK1
Global GNM mode 1
E
PAK1
Global GNM mode 2
F
PAK1
Global GNM mode 3

Figure 3:

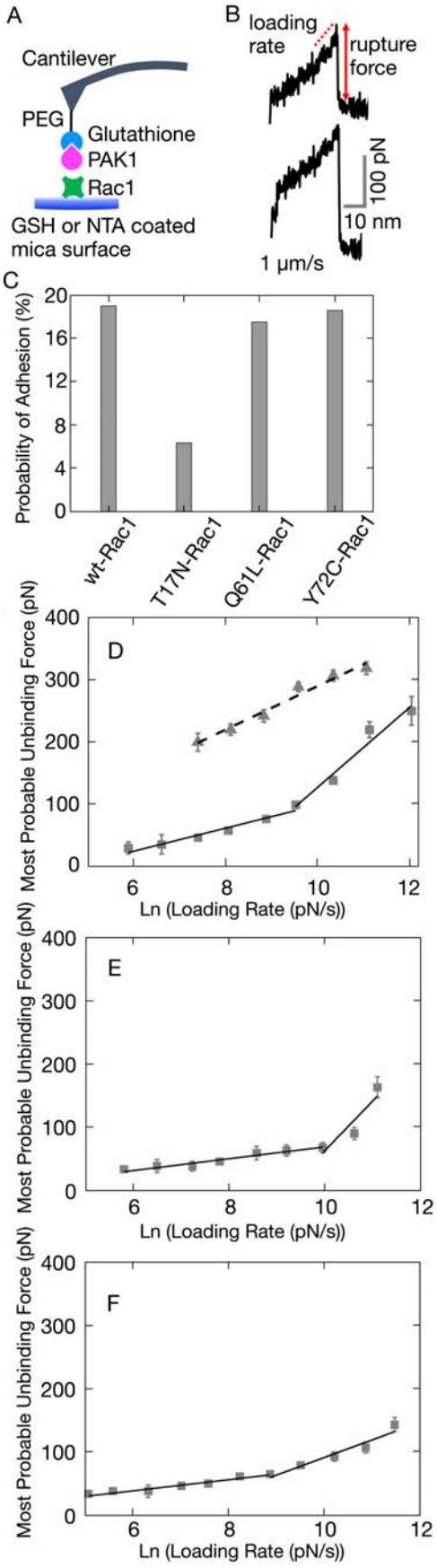
A
Cantilever
PEG
Glutathione
PAK1
Rac1
GSH or NTA coated
mica surface
B
loading
rate
rupture
force
100 pN
10 nm
1 μm/s
C
Probability of Adhesion (%)
20
16
12
8
4
0
wt-Rac1
T17N-Rac1
Q61L-Rac1
Y72C-Rac1
D
E
F
Most Probable Unbinding Force (pN)
400
300
200
100
0
6
8
10
12
Ln (Loading Rate (pN/s))

Figure 4:

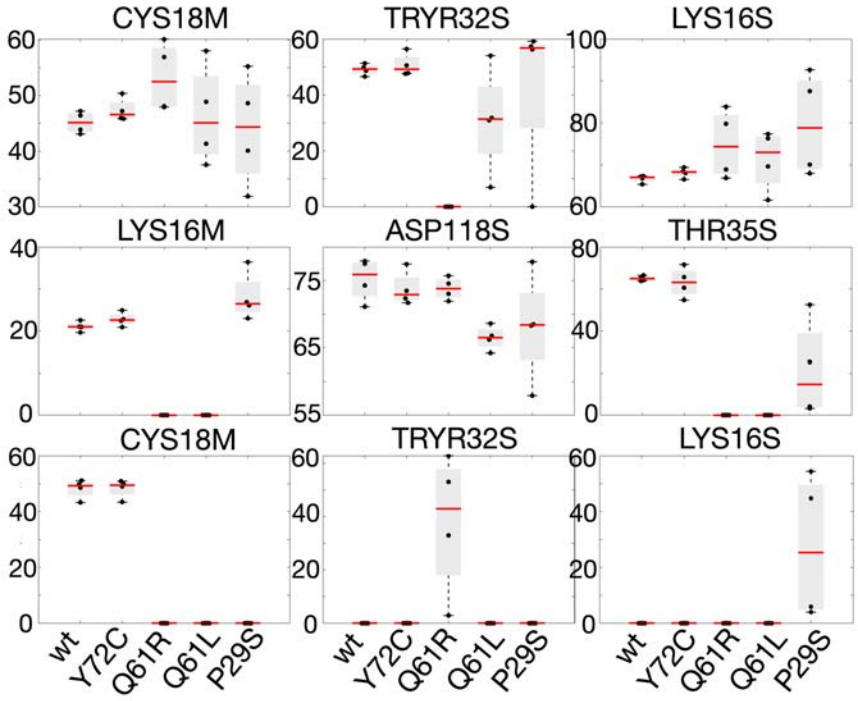
CYS18M
TRYR32S
LYS16S
LYS16M
ASP118S
THR35S
CYS18M
TRYR32S
LYS16S
wt
Y72C
Q61R
Q61L
P29S

Figure 5:

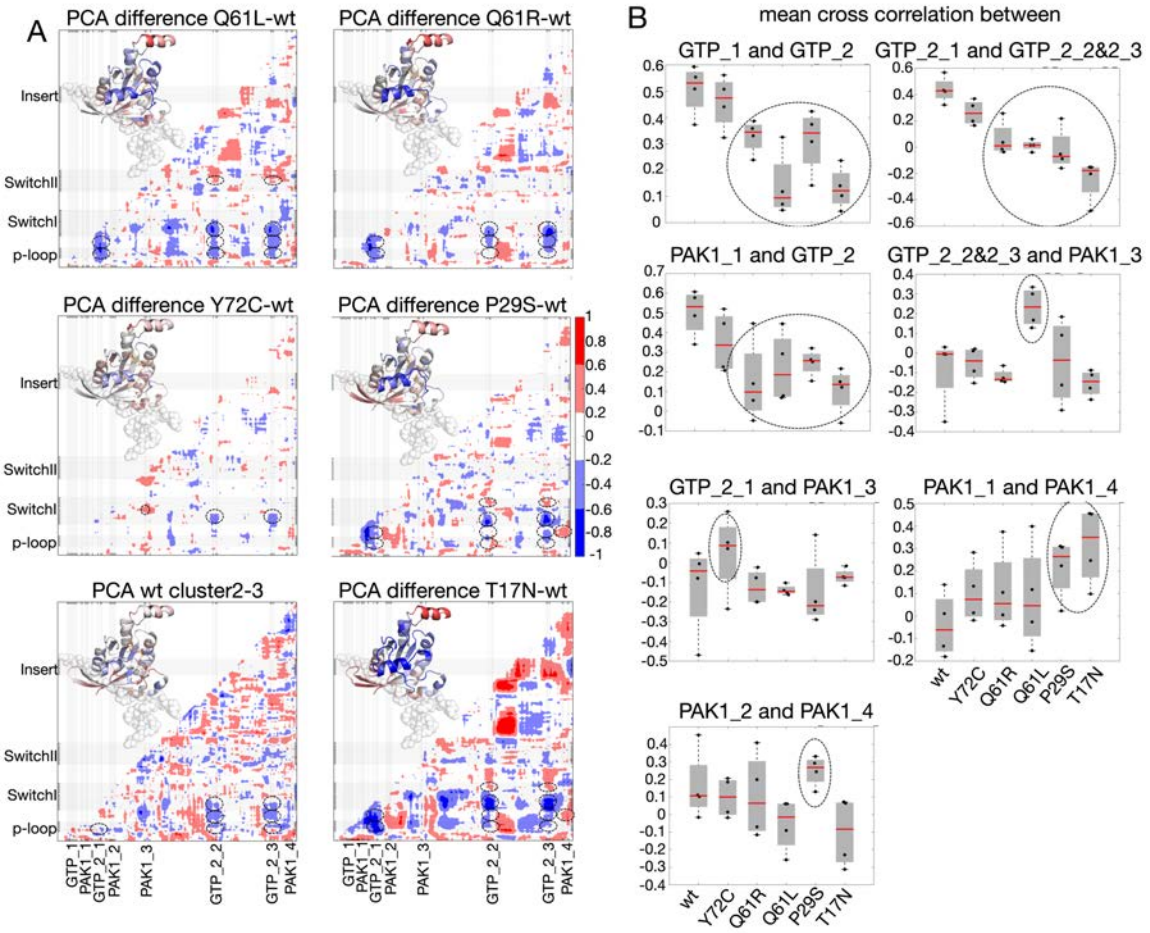
A
PCA difference Q61L-wt
PCA difference Q61R-wt
PCA difference Y72C-wt
PCA difference P29S-wt
PCA wt cluster2-3
PCA difference T17N-wt
Insert
SwitchII
SwitchI
p-loop
GTP_1
PAK1_1
GTP_2_1
PAK1_2
PAK1_3
GTP_2_2
GTP_2_3
PAK1_4
B
mean cross correlation between
GTP_1 and GTP_2
GTP_2_1 and GTP_2_2&2_3
PAK1_1 and GTP_2
GTP_2_2&2_3 and PAK1_3
GTP_2_1 and PAK1_3
PAK1_1 and PAK1_4
PAK1_2 and PAK1_4
wt
Y72C
Q61R
Q61L
P29S
T17N

Supporting Material for

Oncogenic mutations on Rac1 affect global intrinsic dynamics underlying GTP and PAK1 binding

Saliha Ece Acuner[a,b], Fidan Sumbul[a,c], Hamdi Torun[d,*], Turkan Haliloglu[a,*]
[a]Department of Chemical Engineering and Polymer Research Center, Bogazici University, 34342 Istanbul, Turkey.
[b]Present address: Department of Bioengineering, Istanbul Medeniyet University, 34700 Istanbul, Turkey. E-mail: ece.ozbabacan@medeniyet.edu.tr
[c]Present address: U1067 INSERM Parc Scientifique et Technologique de Luminy, 163 avenue de Luminy, 13009 Marseille, France. E-mail: fidan.sumbul@inserm.fr
[d]Department of Mathematics, Physics and Electrical Engineering, Northumbria University, NE1 8ST Newcastle, UK.

*Corresponding Authurs: Turkan Haliloglu and Hamdi Torun
Phone: +90 (212) 359 7002. Fax: +90 (212) 257 5032. E-mail: halilogt@boun.edu.tr
Phone: +44 (191) 227 4746. Fax: +44 (191) 227 3903. E-mail: hamdi.torun@northumbria.ac.uk

SEA and FS contributed equally to this work

ORCID IDs: SEA: 0000-0003-0336-0645; FS: 0000-0002-2250-4280; HT: 0000-0002-7882-286X; TH: 0000-0002-1279-5803

This PDF file includes:

Supporting Text

Materials and Methods

Experimental Methods

Preparation of Molecules and Atomic Force Microscopy (AFM) Setup

The His-tagged wild-type (wt), GST-tagged T17N, His-tagged Q61L and His-tagged Y72C mutant human Rac1 and GST-tagged human PAK1 (p21 binding domain–PBD) molecules, produced in a bacterial expression system, were purchased from Creative BioMart USA, as lyophilized powder. The Tris Buffer solution (containing 50 mM Tris pH 7.5, 0.5 mM $MgCl_2$ and 50 mM NaCl) was prepared in liquid form. GTP molecules were purchased as lyophilized powder from Sigma-Aldrich (St. Louis, MO, USA). In the beginning of each experiment, wt and mutant Rac1 molecules were loaded with freshly reconstituted GTP (in deionized (DI) water to have a final concentration of 2 mM) by preparing the following solution: 0.1-1 mg/ml Rac1, 15mM EDTA and 2mM GTP. After 30 minute incubation at room temperature, 60 mM $MgCl_2$ (final) was added to lock Rac1 and GTP molecules. Polyethylene glycol (PEG) and Glutathione (GSH) attached Si_3N_4 (silicon nitride) AFM probes, as well as NTA (Nitrilotriacetic acid) and GSH covered mica surfaces were purchased from Novascan Technologies, Inc., USA. The nominal spring constants of the cantilevers used in the experiments are 0.01 and 0.1 N/m. The experiments were performed using a commercial AFM system (Dimension Edge, Bruker Nano, Santa Barbara, CA, USA).

Immobilization of Rac1 Molecules and Functionalization of AFM Tips with PAK1

In all of the pulling experiments, PAK1 was functionalized on AFM tip and wt/mutant Rac1 molecule was immobilized on the functionalized mica surface via physical adsorption. GST is adsorbed to GSH and His is adsorbed to NTA. Thus, GSH and NTA mica surfaces respectively were used to functionalize GST-tagged T17N and His-tagged wild-type (wt), Q61L and Y72C mutant human Rac1 (Figure 3A).

Wild-type and mutant Rac1 molecules (100 µl from each with 20 µg/ml in Tris) were immobilized on the mica surface through 30-minute incubation at room temperature. 50 µl of EDTA and GTP (solution with deionized (DI) water) was also added for GTP loading of Rac1 molecules, so that GTP-loaded Rac1 molecules got attached to the mica surface. After the incubation, the mica surface was gently rinsed with DI water to remove unbound/loosely bound molecules. The mica surface with immobilized molecules was kept hydrated via Tris prior to data collection.

Functionalized cantilevers (GSH and PEG attached) were dipped into the 100 µl GST-tagged PAK1 (20 µg/ml in Tris buffer) and incubated for 30 minutes at room temperature, then gently rinsed two times with DI water to remove unbound/loosely bound PAK1 molecules. PAK1 functionalized AFM tips were then used immediately in force measurements. Figure 3A shows the multi-step functionalization of AFM tip and surface in this experiment. Multi-step functionalization of AFM tips may introduce measurement of unbinding forces that do not arise from the molecules of interest. To test the existence of such undesired unbinding events, the pulling experiments were performed using: 1) PEG + Glutathione attached tip and NTA covered mica surface, 2) PEG + Glutathione + PAK1 attached tip and NTA covered mica surface, 3) PEG + Glutathione attached tip and NTA + Rac1 covered mica surface. No statistically significant specific adhesion was observed between multi-step functionalization elements (see Figure 3B). Additionally, in order to minimize random errors such as variation in surface coverage, the data was collected at different locations on the surface.

Experimental Procedure

Three different sets of AFM pulling experiments were performed to investigate the unbinding force distributions involved in the interactions of Rac1-PAK1 complexes. Figure 3A shows the experimental setup for the Rac1-PAK1 systems. All force measurements were performed in the fluid-phase at room temperature. Cantilevers were calibrated using thermal noise method (1). AFM pulling experiments, the multi-functionalized AFM tip coated with p21 binding domain of PAK1 was brought in contact -manipulated by a piezo- with Rac1 adsorbed surface (immobilization and functionalization details are described above). The deflection signal, which gives the position of the AFM cantilever, was recorded during the experiment. To obtain the unbinding forces at various loading rates, force-distance data were recorded at different approach/retract velocities -spanning three order of magnitudes- (0.1, 0.5, 1, 2.5, 5, 10, 20, 50,

100 μm/s). At each velocity, we collected statistically significant number of force-distance data for further analysis. The trigger force was fixed to 2 nN.

The unbinding force at a specific loading rate was determined by inspecting the force-extension curve. The effective loading rates were estimated by fitting a linear line to the force-time curve immediately before the rupture point in each approach/retract. The effective loading rates obtained from the experiment were equally quantized in the logarithmic space to get uniform number of most probable rupture force vs logarithm of loading rates relation (2, 3). Force distributions are plotted as histograms for each loading rate-range- and the most probable rupture force at each loading rate is determined by inspecting the force histograms. The most probable rupture force of the Rac1-PAK1 complex at a given loading rate interval was determined by calculating the median of the force histograms. The most probable rupture force f^*, versus the natural logarithm of the loading rate, $\ln(r_f)$, was plotted and the Bell parameters (k_{off} and x_β; where k_{off} is the unbinding rate constant and x_o is the distance from the bound state of the activated state), which are characteristic values of the investigated molecular pair, were estimated from the slope, $\frac{k_BT}{x_\beta}$, and the intercept, $\frac{k_BT}{x_\beta}k_{off}$, of the fitting linear curves (See Eq. S1).

$$f^* = \frac{k_BT}{x_\beta}\left(ln\, r_f - \ln\frac{k_BT}{x_\beta}k_{off}\right) \qquad \text{(Equation S1)}$$

where k_B and T are the Boltzmann constant and the absolute temperature, respectively.

Computational Methods

Gaussian Network Model (GNM) and Mutation Mapping on Hinge Sites

In the Gaussian Network Model (GNM) approach, a protein is represented as a network of amino acids that are assumed to undergo Gaussian-distributed fluctuations around their mean positions. In this network, nodes are α-carbon atoms and edges are the springs (with a uniform force constant γ) combining residues within a cutoff distance (e.g. r_{cut} = 10 Å, in our case) (4, 5). Mean-square residue fluctuations (GNM normal modes) and correlations between them can be calculated by diagonalizing the inverse Kirchhoff (connectivity) matrix, the eigenvalues of which are proportional to the corresponding mode's frequency of motion. Global and local motions correspond respectively to low-frequency (slow) modes and high-frequency (fast) modes. In a given slow mode, the point at which there is a change in the sign of correlation values is defined as a "hinge site" (6) and these points generally overlap with the minima of the corresponding slow-mode shape. GNM calculations are done via Python 2.7 (7) for the three slowest modes. Data from COSMIC and cBioPortal (8-10) are combined and mapped to the wt Rac1 structure (PDB ID: 3th5) to observe what portion of the disease-related mutations is within 4.2 Å proximity of the hinge sites for these three slowest modes. The distance calculation is done by PyMOL (The PyMOL Molecular Graphics System, Version 2.3.2 Schrödinger, LLC.) through measuring the center of atom distances of hinge residues and their nearby residues.

Molecular-Dynamics (MD) Simulations

The starting structures for molecular-dynamics (MD) simulations were the GTP-bound wild-type Rac1 (PDB ID: 3th5), Q61L mutant Rac1 (PDB ID: 4gzl), P29S mutant Rac1 (PDB ID: 3sbd), Q61R and Y72C mutant Rac1 (*in silico*) and nucleotide free T17N mutant Rac1 (PDB ID: 3b13). To obtain GTP-bound structures, starting coordinates were modified by changing the β-γ bridging nitrogen atom of GNP (a non-hydrolyzable analog of GTP) with oxygen. The *in silico* mutations of the wild-type Rac1 (PDB ID: 3th5), Y72C and Q61R, were created using VMD 1.9.1 (11). The Q61L mutant Rac1 structure (PDB ID: 4gzl) lacks residues 31 and 48, which were modeled using the wild-type structure (PDB ID: 3th5).

A total of 2.4 μs-long MD simulation, including (100 ns-long) four parallel runs for the wild type and five mutant Rac1 structures, was performed for the wild-type and mutant Rac1 structures (details in Table S1). The frames for equilibration were decided based on the Root Mean Square Deviation (RMSD) (Figure S5). All-atom CHARMM36 force field (12) of NAMD 2.7 (13) was used taking integration time step as 2 fs with periodic boundary conditions. The temperature and pressure were maintained at 310 K (with a Langevin damping coefficient of 1 ps^{-1} (14)) and at 101.3 kPa (by means of Nosé-Hoover Langevin piston pressure control), respectively. The length of bonds of hydrogen atoms were restrained by the SHAKE algorithm

(15). TIP3P-type water box with at least 10 Å of padding was used for the crystal structures (16). Cl^- and Na^+ ions were used to neutralize the system. For nonbonded Lennard-Jones interactions, the switching function started at 10 Å; a cutoff of 12 Å was used and the nonbonded pair list distance was 14 Å. The particle-mesh Ewald method was employed for the long-range electrostatics (17). The conjugated gradient method was used for steric crush and crystal contact removal. MD trajectories were saved every 10 ps and then analyzed by considering the average of four parallel 100 ns simulations for each case, including calculations of the Root Mean Square Deviation (RMSD) and Mean Square Fluctuation (MSF) profiles, principal component analysis (PCA) for cross-correlations (including 10 modes), dihedral angles and hydrogen bonding. The softwares used for the analyses were VMD 1.9.1 (11), MATLAB R2015a (The MathWorks, Natick, MA) and Python 2.7.

H-bonding and distance calculations

We analyzed the changes in hydrogen bonding (H-bonding) occupancy percentages during the simulations between Rac1-GTP and within Rac1 considering both backbone and side chain atoms of residues. The average of the H-bond occupancy values was considered as significant if the corresponding occupancy is higher than 10% in two or more of the four parallel MD simulations in each case. The H-bond occupancies of mutants are compared to the wild-type by taking differences of average H-bonding occupancy values for residue pairs and again considering only the values greater than 10% as significant changes. Distances between residues as well as GTP and Mg^{2+} ion are calculated by using open source VMD script *distance.tcl*, which calculates the distance between the center of mass of two selections for every frame.

Clustering the simulated Rac1 structures and structural modeling of Rac1-PAK1 complexes

The generated equilibrated trajectories through MD simulations are also clustered based on mutual RMSD (r_{cut} = 1.5Å) using unsupervised k-means clustering to distinguish different ensembles explored via simulations. MMTSB toolset is used to cluster the ensemble of simulated trajectories. The complexes of the representative Rac1 conformations (best members closest to the cluster centroid) from each simulated system (wt, Q61L, Q61R, Y72C, P29S, T17N Rac1) with the available PAK1 structure (PDB ID: 1e0a) are modeled to analyze the effects of mutations on the binding properties of Rac1-PAK1 complex structures. PRISM server (18, 19) is used for structural modeling and the structure of Cdc42 (another member of the Rho family of GTPases)-PAK1 (PDB ID: 1e0a) is used as the template structure and the GTPase binding domain of PAK1 in this structure (PDB ID: 1e0aB) is used as one of the targets, whereas the cluster representatives from the simulated wt and mutant Rac1 structures are used as the other target structure. The predicted binding energies of the modeled complex structures are estimated by the global binding energy calculated at the end of the flexible refinement step of PRISM algorithm by employing FiberDock (flexible induced-fit backbone refinement in molecular docking) (20). FiberDock scores and rank the putative complexes by including a variety of energy terms, such as desolvation (atomic contact) energy, vdW interactions, partial electrostatics, hydrogen and disulfide bonds, π-stacking and aliphatic interactions. Moreover, the free energy of assembly dissociation ΔG^{diss} (in kcal/mol) values of the modeled complex structures are predicted by PDBePISA (Proteins, Interfaces, Structures and Assemblies) server (21).

Results and Discussion

Clusters of Rac1

We compare the two distinct states (state 1 and state 2, referring to strong/weak unbinding forces and low/high rate of PAK1 dissociation) of Rac1-PAK1 complex via SMFS experiments, with the clusters of isolated Rac1 MD sampled conformations in the wt-Rac1 in terms of predicted binding free energies through docking and similarity of dynamics with respect to the mutants (as will be discussed below). Based on the predicted interaction energies via Rac1-PAK1 docking analysis, one of the wt Rac1 clusters (referred as state 1) displays stronger interactions than the other one (state 2) (Table 2). Besides, the GTP-binding residues have weakened correlations with each other in state 1 with respect to state 2 of the wt Rac1 (Figures 6 and S14). Moreover, majorly or single clustered mutants' correlation differences from state 2 of the wt Rac1 yield

similar results to wt Rac1's own cluster differences (state 1–state 2), such that the GTP-binding residues have weakened correlations with each other (Figures 6 and S14).

The mostly populated P29S mutant Rac1 cluster (referred as state 1) also displays stronger interaction energies than the next highly populated one (referred as state 2). In terms of correlations, the main difference observed among the P29S clusters is for the correlations of the region between p-loop and Switch I (including PAK1-binding residues) with GTP-binding residues 158-160. This cooperativity decreases more for state 1 of P29S more (Figure S14). Highly mobile Switch I may account for this decrease in the cooperativity. The other mutant clusters are not mentioned here as single cluster behaviors are identical to the average cases.

There is no clear distinction between the clusters corresponding to the two most populated states of the wild-type and Q61L Rac1 in terms of H-bond occupancy with GTP. On the other hand, two distinct behaviors are observed for P29S: increased total number of H-bonds (within protein as well as with GTP) is observed for one of the P29S clusters (state 1). For example, although the H-bond occupancy is significantly lost for GTP-T35 (side), a complementary H-bond forms between GTP-T35 (main) specific to the P29S in this cluster (Figure S15). Moreover, Switch I region has the highest mobility with respect to the state 2 of P29S as well as other mutant and wt Rac1 clusters and mobile Switch I contributes to the loss of correlated motions among the GTP-binding residues as observed in the average cases (without clustering) discussed above. For the other cluster of P29S (state 2), H-bonds with GTP-Y32 and GTP-T35 totally disappear, which can be explained with the significantly higher side chain orientational fluctuations with respect to state 1 of P29S as well as the wt and other mutants (except Q61L) (Figure S15).

To sum up, state 1 of P29S is similar to state 1 of the wt Rac1 in terms of correlations and state 2 of the P29S is similar to constitutively active Q61L mutant (cluster 1) in terms of H-bonds. It was suggested that fast-recycling mutants (e.g. P29S Rac1) might be more efficient oncogenic drivers than constitutively active mutants (e.g. Q61L Rac1) due to their ability to mimic normal signaling by being able to associate with/dissociate from effectors (22).

Rac1-PAK1 Model Complexes: States 1 and 2 of wt Rac1

We model the top ten representative Rac1 conformations (best members of the MD sampled conformations closest to the cluster centroid) from each simulated system (wt, T17N, P29S, Q61L, Q61R, Y72C Rac1s) with the available crystal structure of PAK1 (PDB ID: 1e0a) to analyze plausible effects of the mutations on the binding behavior of Rac1 with PAK1. We compare these modelled complex structures with PAK1 to see the inter-cluster differences in terms of the average predicted binding energy (20) and free energy of dissociation (ΔG_{diss}) (21), together giving hints on the binding strength. Note that, the wt and mutant Rac1 structures largely resemble each other except a few mutant residues, some of which are not directly at the interface but have allosteric effects. As such, the consistency of these arbitrary scores can give only hints about the binding strength tendency of clusters but they are not precise comparison measures on their own. Although inactive T17N mutant Rac1 is unable to bind to PAK1, the best ten members of its major cluster (60%) were also modeled with PAK1 to have reference values for average predicted binding free energy and free energy of dissociation. The results show that all other mutant and wt Rac1-PAK1 complexes are more favorable than the inactive T17N Rac1-PAK1 complex, as expected (Tables 2 and S2).

Similarly, P29S clusters (with 71% and 25%) display state 1 and state 2 such that the average global binding energies are -97 and -82 with average ΔG_{diss} values 5.6 and 3.8 (kcal/mol), respectively (Tables 2 and S2). However, Q61L have two major clusters (68% and 17%) and the distinction between state 1 and state 2 cannot be observed as clearly as the wt and P29S due to inconsistent binding behavior of the clusters (with lower predicted binding energy (stronger binding) but also lower ΔG_{diss} (easier dissociation)). This is also the case in the SMFS experiments such that a single conformational/dynamical state is observed for Q61L.

The simulated structures of the other active mutants Q61R and Y72C Rac1s fall into a single cluster and form complexes with PAK1 with average binding energies of -96 and -91, respectively, and ΔG_{diss} value of 5.9 (for both, in kcal/mol) generally in between the state 1 and

state 2 of the wt Rac1-PAK1 complexes Tables 2 and S2). However, note that the predicted binding energies and ΔG_{diss} values for the top ten members of these mutants span a wide range. Although there are complexes with values closer to state 1, the complexes with the opposite behavior level out and the average falls in between (see Table S2 for the energy predictions of the complexes with all top ten members).

Supporting Figures

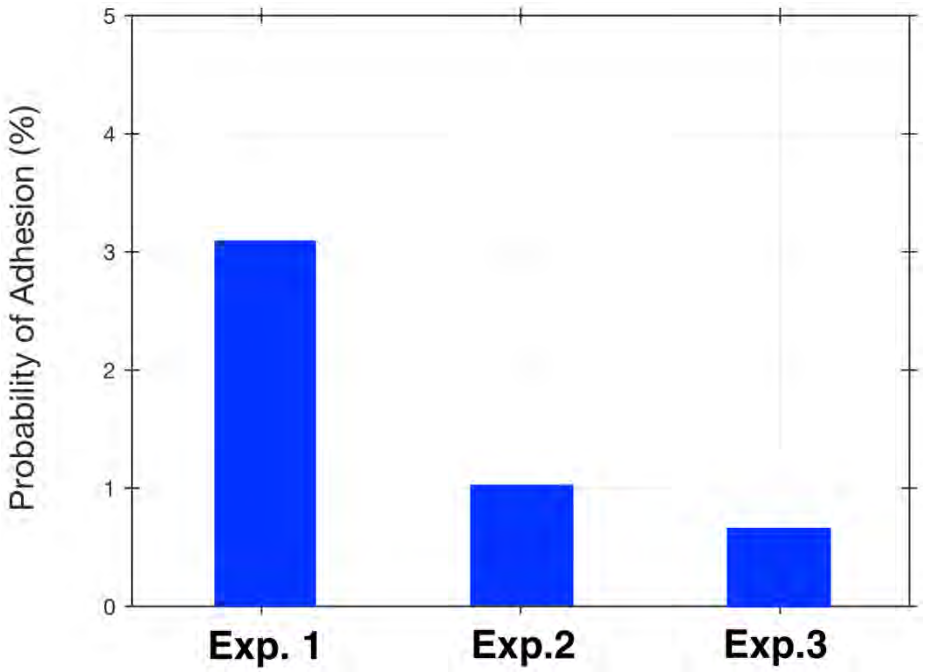

Figure S1. The probability of adhesion obtained from control experiments of multi-step functionalization. Three different experiments were conducted to ensure the specificity of measured forces coming from the molecules of interest. Exp.1 is the pulling experiment of PEG + Glutathione attached AFM tip and NTA covered mica surface, Exp.2 is the pulling experiment of PEG + Glutathione + PAK1 attached tip and NTA covered mica surface, Exp.3 is the pulling experiment of PEG + Glutathione attached tip and NTA+Rac1 covered mica surface.

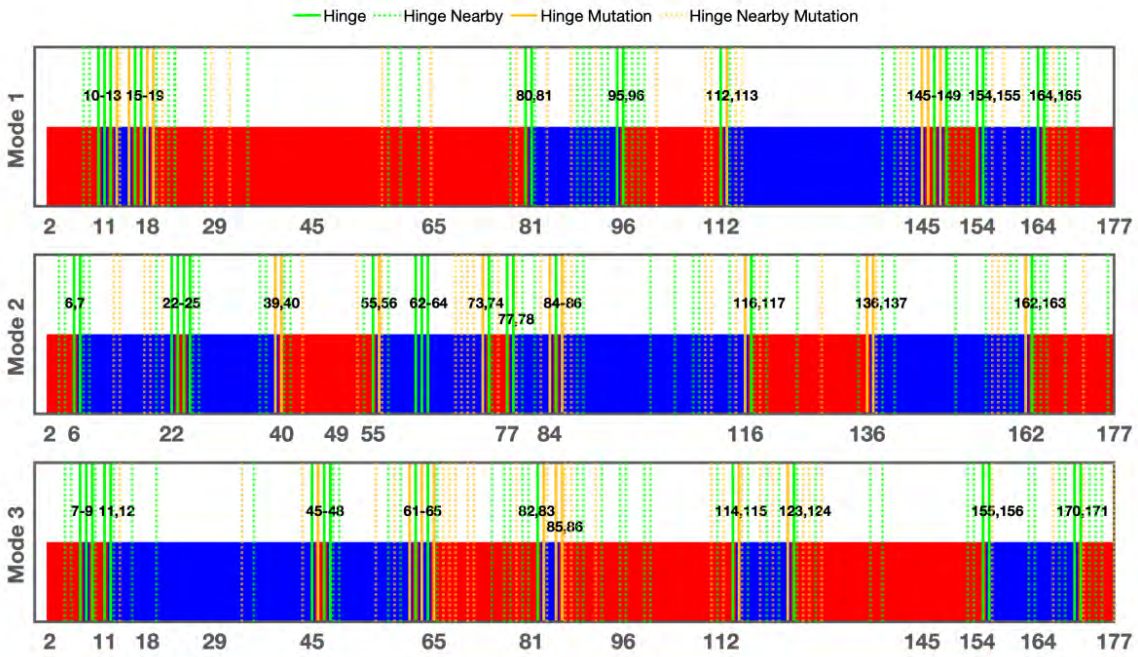

Figure S2. 2D representation of Rac1 oncogenic mutations corresponding to the hinge axes of the first three slowest global modes of motion revealed by GNM. Red and blue regions display two dynamic domains moving in opposite directions. Green lines are hinge residues on Rac1 and green dashed lines are nearby residues in 4.2 Å proximity to hinge residues. Orange lines are oncogenic mutations corresponding to hinge residues and orange dashed lines are oncogenic mutations that are in 4.2 Å proximity to hinge residues.

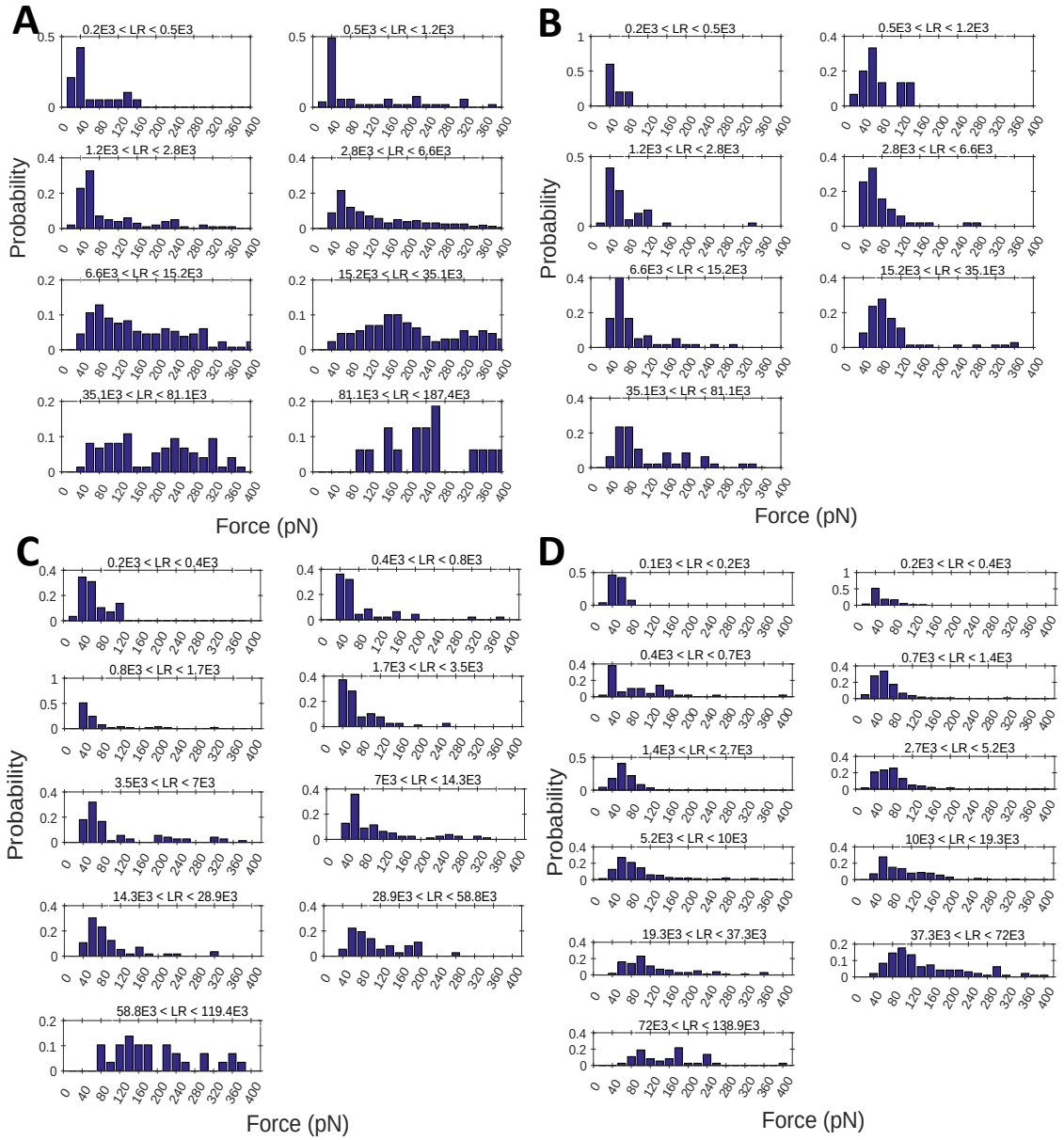

Figure S3. Adhesion force histograms at different loading rates obtained from AFM pulling experiments at room temperature. (A) GTP loaded wild-type Rac1-PAK1 complex. (B) GTP loaded T17N Rac1-PAK1 complex (C) GTP loaded Q61L Rac1-PAK1 complex (D) GTP loaded Y72C Rac1-PAK1 complex. At higher loading rates (except the highest one) a bimodal distribution was observed for GTP loaded wild-type Rac1-PAK1 complex, which could be associated with different conformational or dynamic states of the complex.

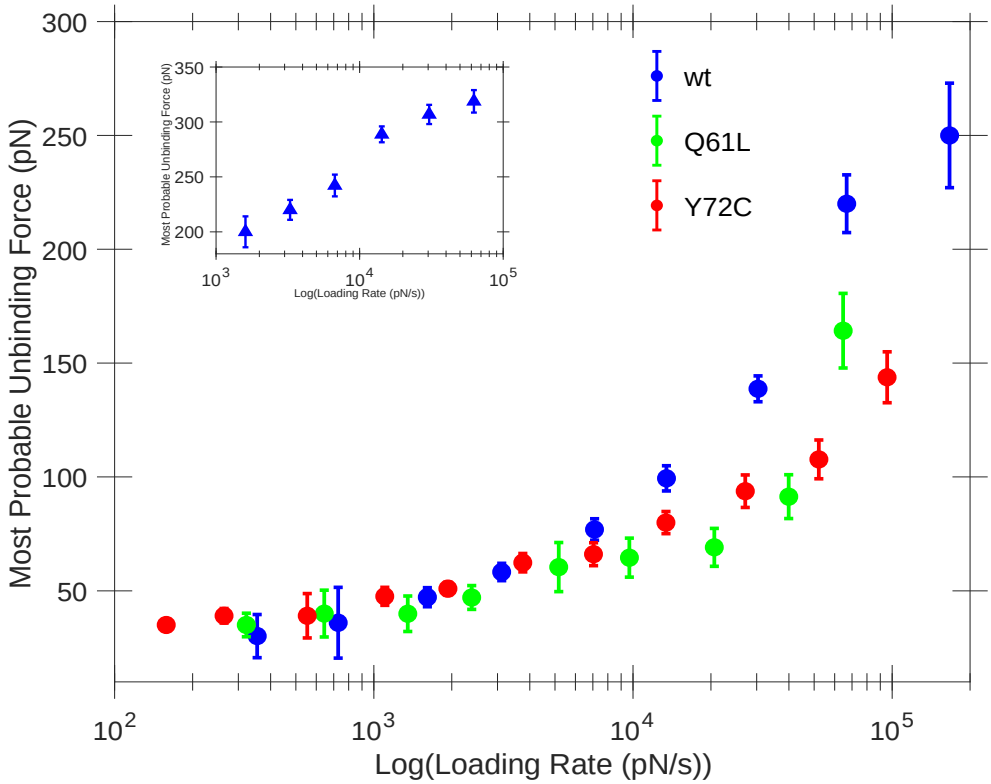

Figure S4. The most probable rupture forces observed along the measured loading rates. Wild-type Rac1-PAK1 dissociation exhibits two different states, state 1 (given inset) and state 2, where Q61L and Y72C Rac1-PAK1 dissociation shows single state which directly maps to state 2 of wild-type Rac1-PAK1 dissociation. The unbinding forces measured at lower loading rates are similar in all cases. However, as the loading rate increases, the rupture force measured in state 2 wild-type Rac1-PAK1 complex is higher than the mutants. Steeper increase in the rupture forces results in higher dissociation constant and therefore faster dissociation. Therefore, the lifetime of wild-type Rac1-PAK1 complex is shorter than both oncogenic and constitutively active mutants.

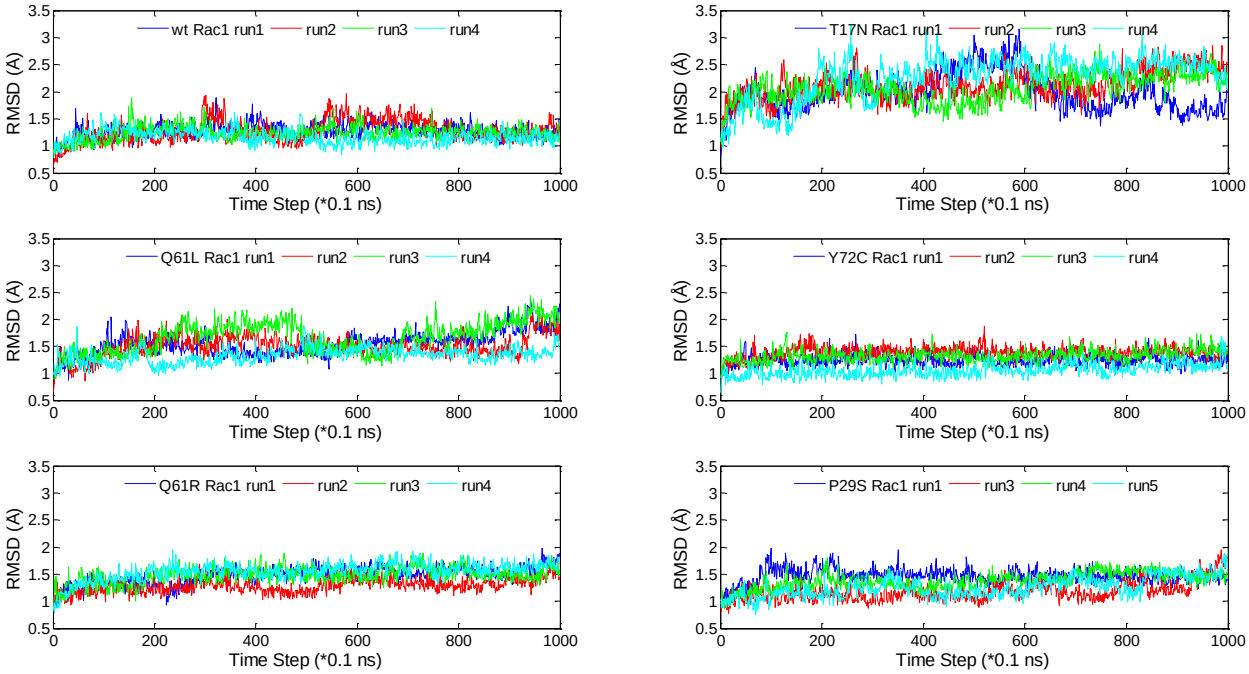

Figure S5. RMSD profiles during parallel MD simulations for the wild-type and mutant Rac1 structures.

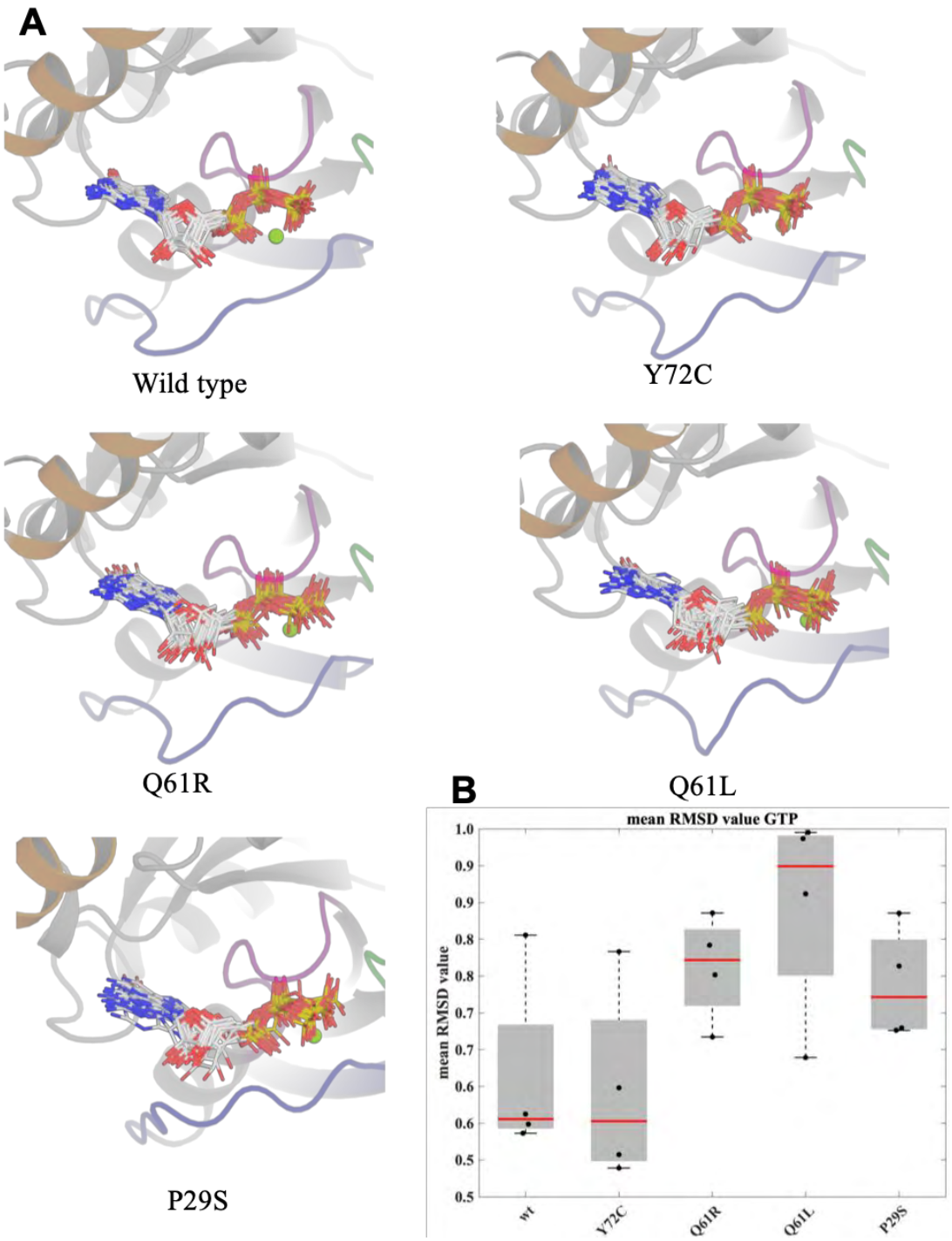

Figure S6. (A) The positional fluctuation of GTP in all simulated trajectories with 10 ns time intervals is shown. Alteration in H-bonding networks results in higher positional fluctuation of the phosphate tail of GTP in all mutations (especially Q61L). All four parallel equilibrated simulation trajectories are combined and aligned on wt Rac1 structure. The functional regions are color coded as in previous Figures. (B) Box plot of the mean value of the RMSD of GTP calculated over each trajectories by aligning the protein backbone. The red line defined the median of the mean RMSD of GTP over the parallel runs. The mean RMSD value of individual parallel runs are shown as black circles. The grey boxes show the 25th and 75th percentiles. No outliers are considered.

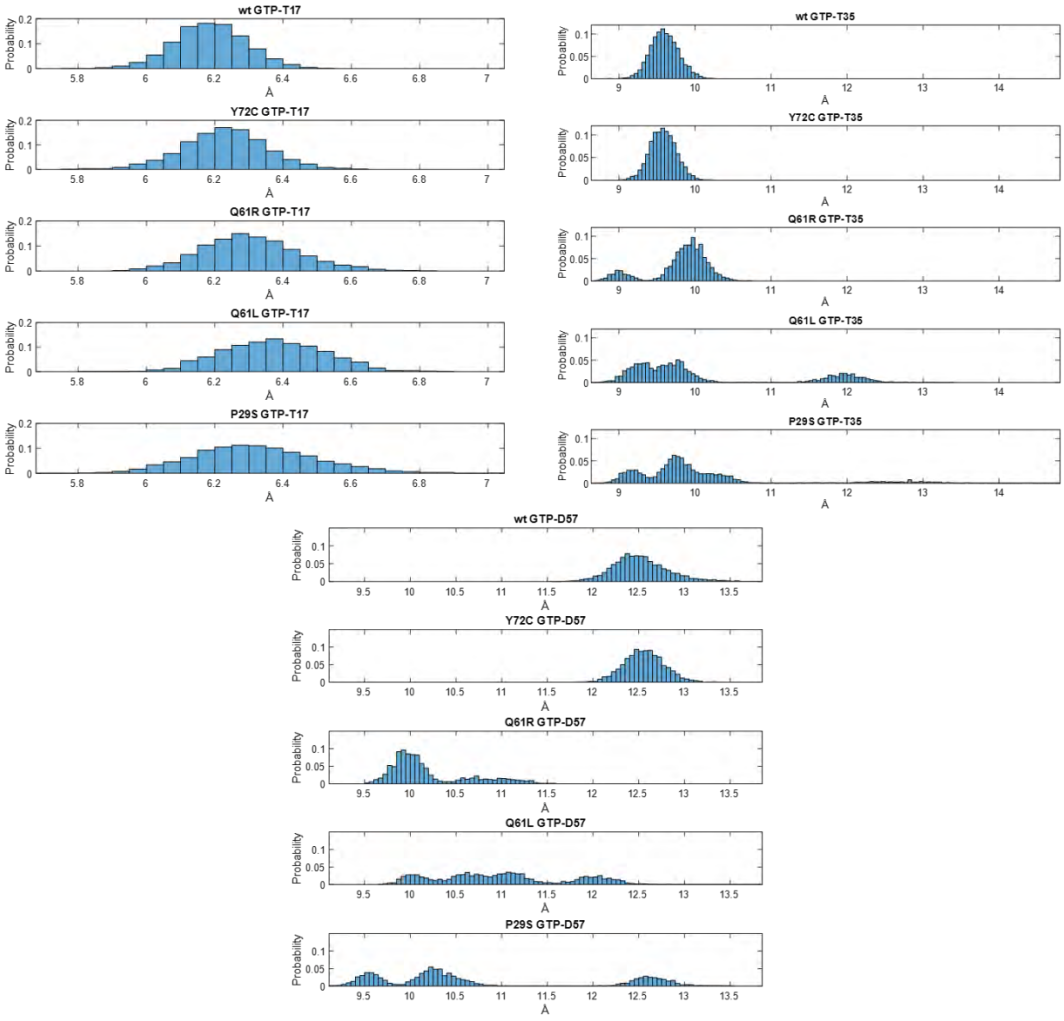

Figure S7. The distribution of distances (in Å) between GTP-T17, T35 and D57 residues in simulations of wt and mutant Rac1 structures.

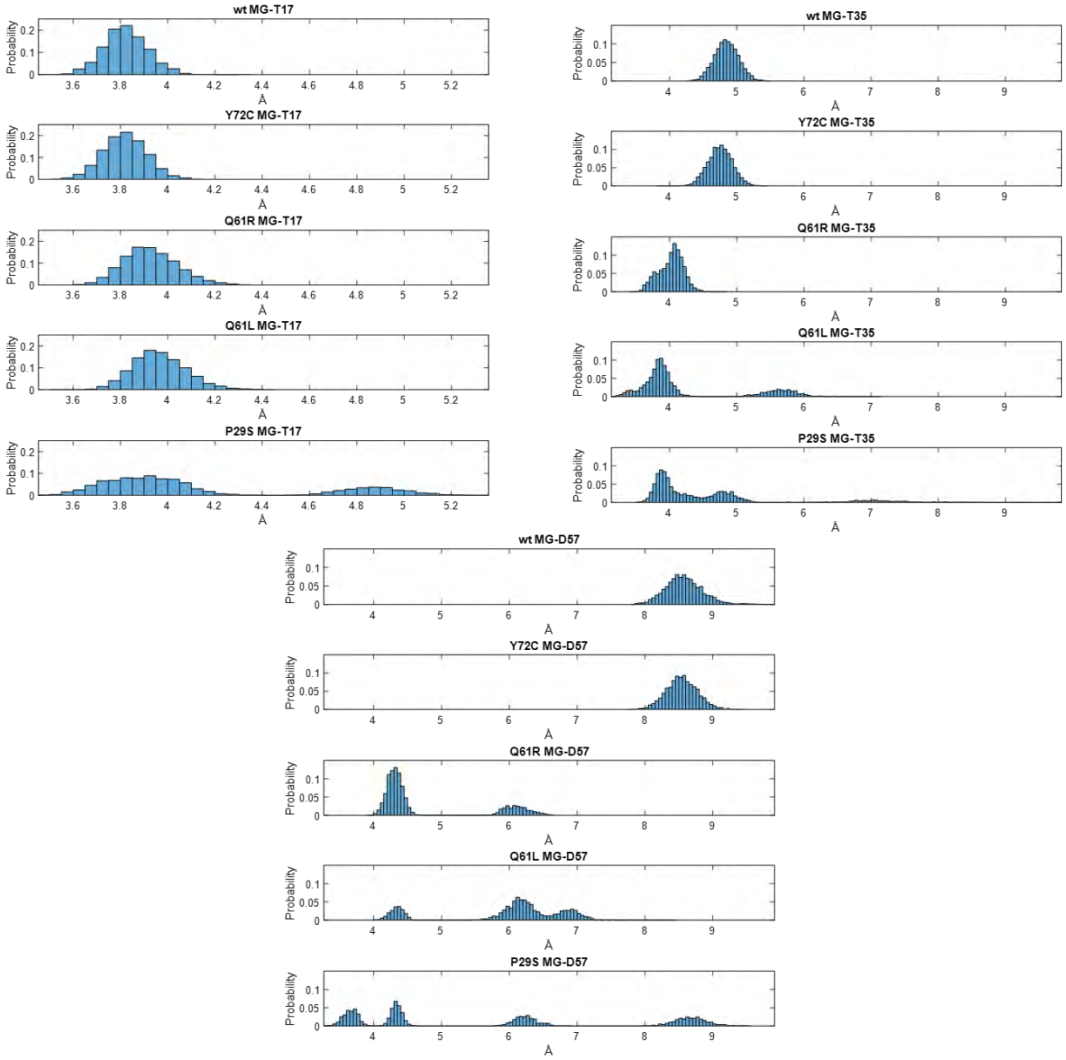

Figure S8. The distribution of distances (in Å) between Mg^{2+} ion-T17, T35 and D57 residues in simulations of wt and mutant Rac1 structures.

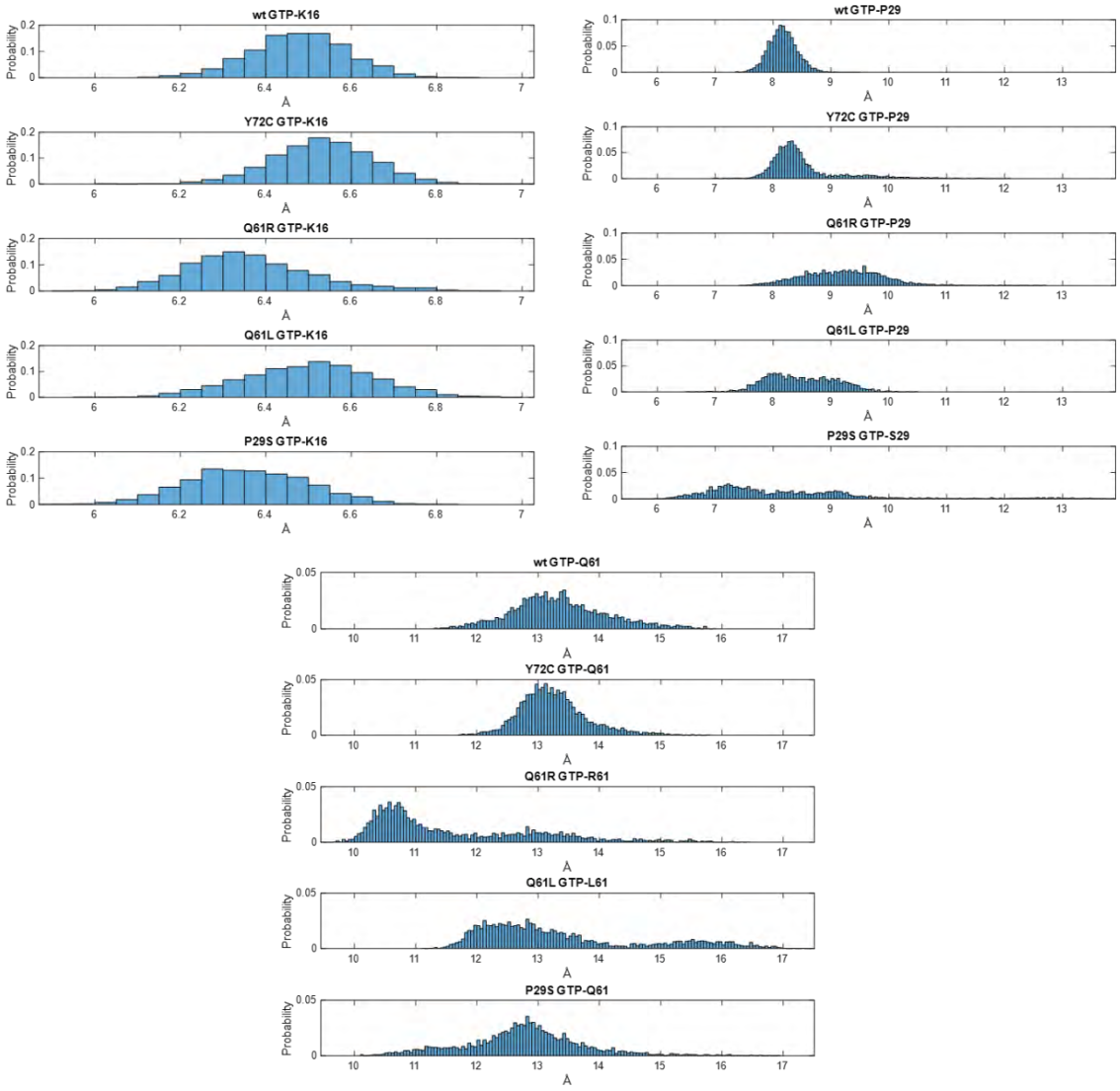

Figure S9. The distribution of distances (in Å) between GTP and K16, P/S29 and Q/R61 in simulations of wt and mutant Rac1 structures.

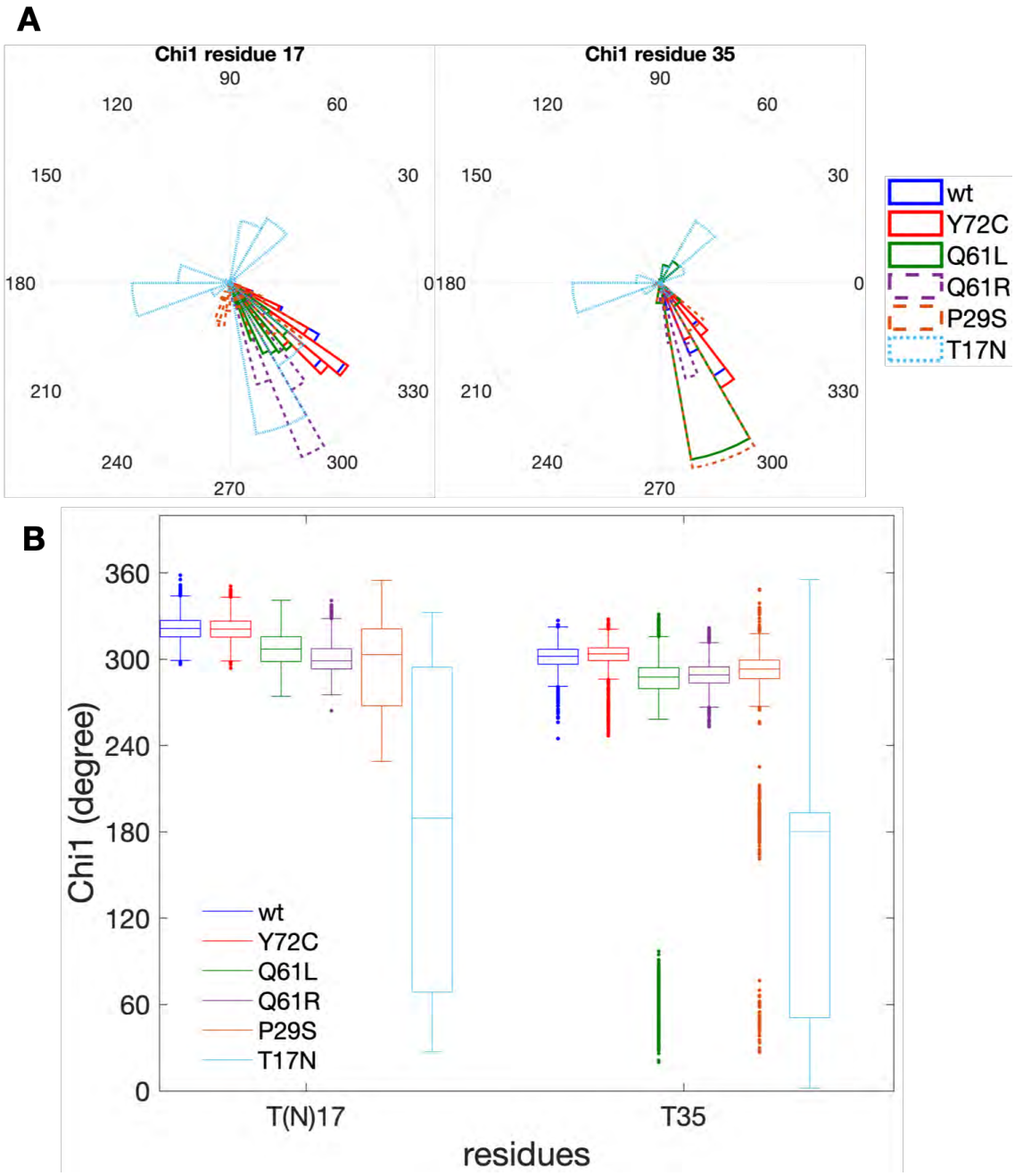

Figure S10. The ensemble of side chain conformational sampling of T17 and T35 which coordinates Mg+2 ion functions as a gate-keeper in all simulated trajectories. (A) Histograms of the angles in circular coordinates. The histograms are normalized with total number of conformations obtained with all parallel simulations of each case. (B) The box plot of the corresponding angles throughout the trajectories.

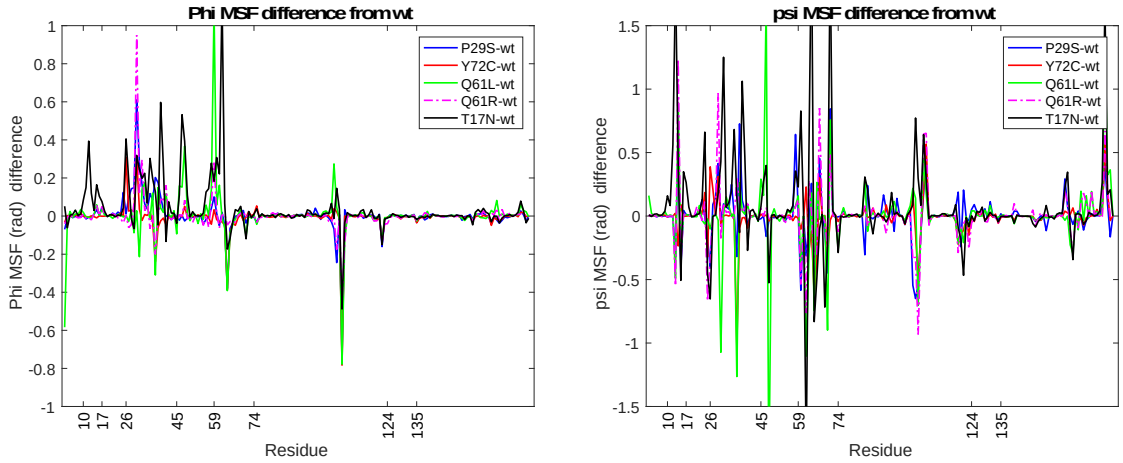

Figure S11. The deviation in the mean square fluctuations (MSF) of the backbone dihedral angles of all the studied mutant Rac1s with respect to wt Rac1. The most profound deviations are observed in the switch loops upon mutations. Although some local increased rigidities are observed in these regions, they are mostly superseded by forerunner increased flexibility.

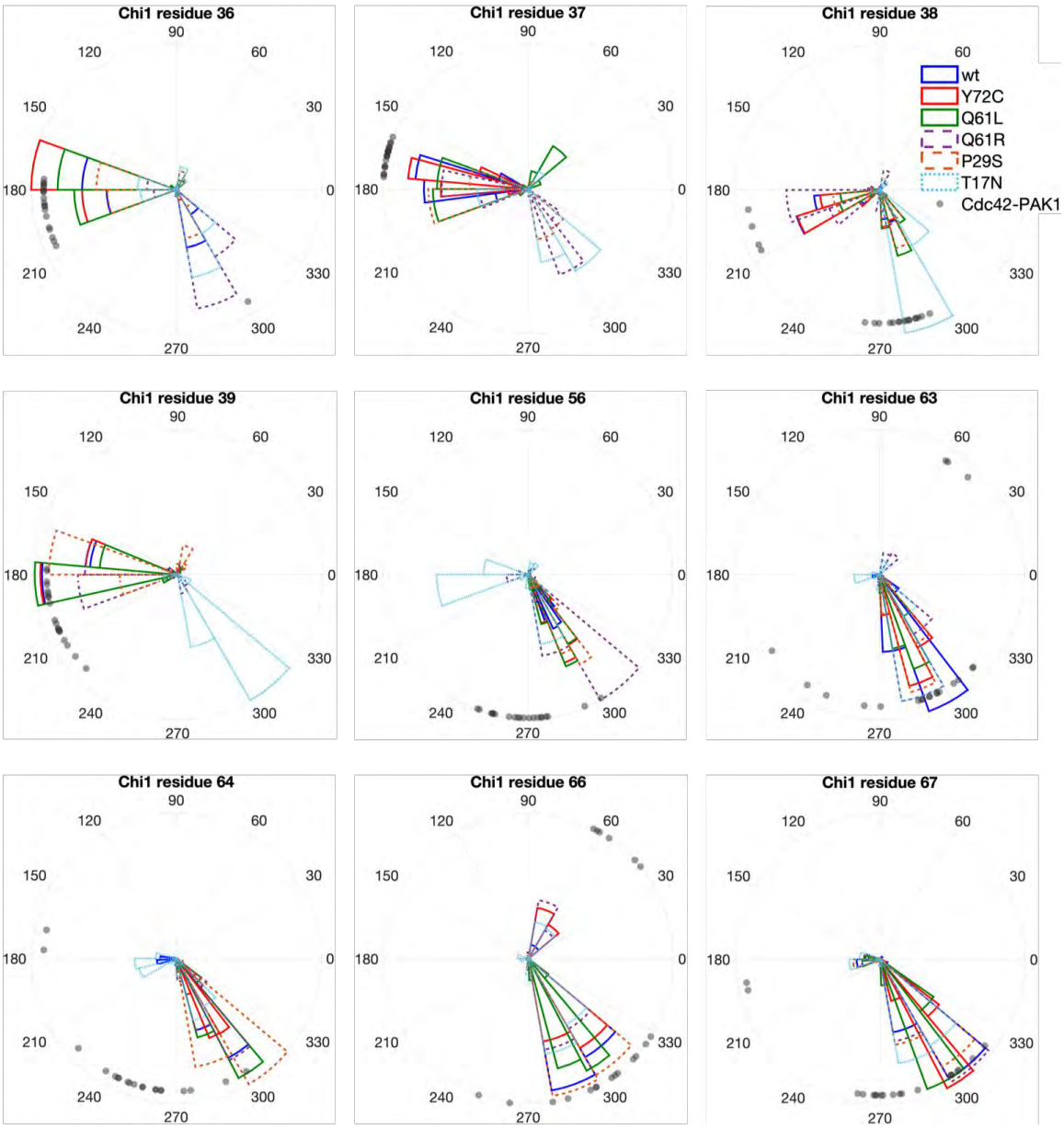

Figure S12. The ensemble of side chain conformational sampling of V36, F37, D38, N39 on Switch I; N63, Y64, R66 and L67 on Switch II and W56 on Rac1 which are common in GAP, GEF and PAK1 binding sites in all simulated trajectories and the 20 NMR complex structure of Cdc42-PAK1. The histograms are normalized with total number of conformations obtained with all parallel simulations of each case. The differences in the side chain orientations of V36, F37, Y64, R66 and L67 are allosterically altered by studied mutations. Observed alterations explain how these mutations determined the binding partner as well as the strength of the complex.

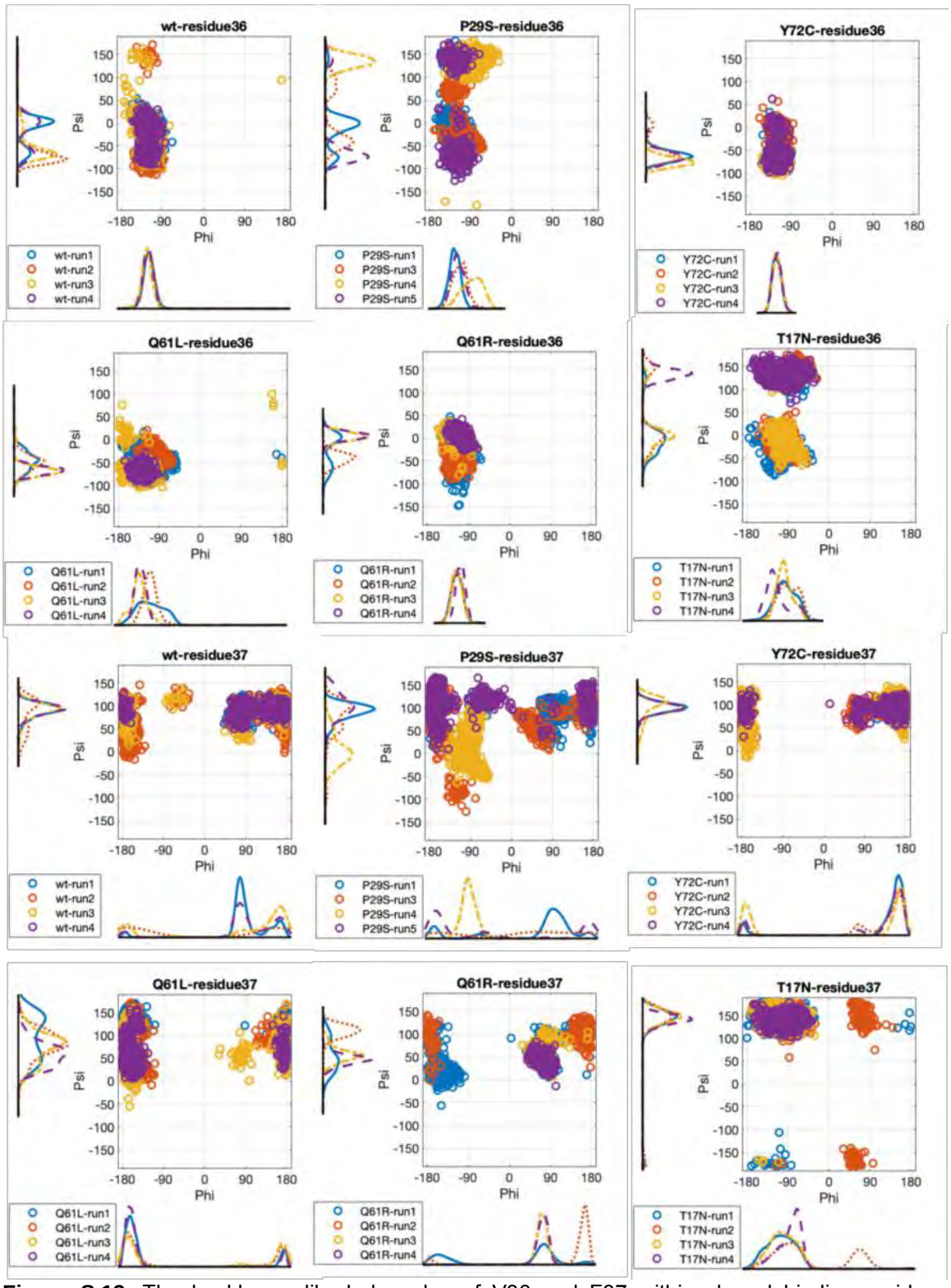

Figure S.13. The backbone dihedral angles of V36 and F37 within shared binding residues among upstream/ downstream binding partners of Rac1 in different simulations.

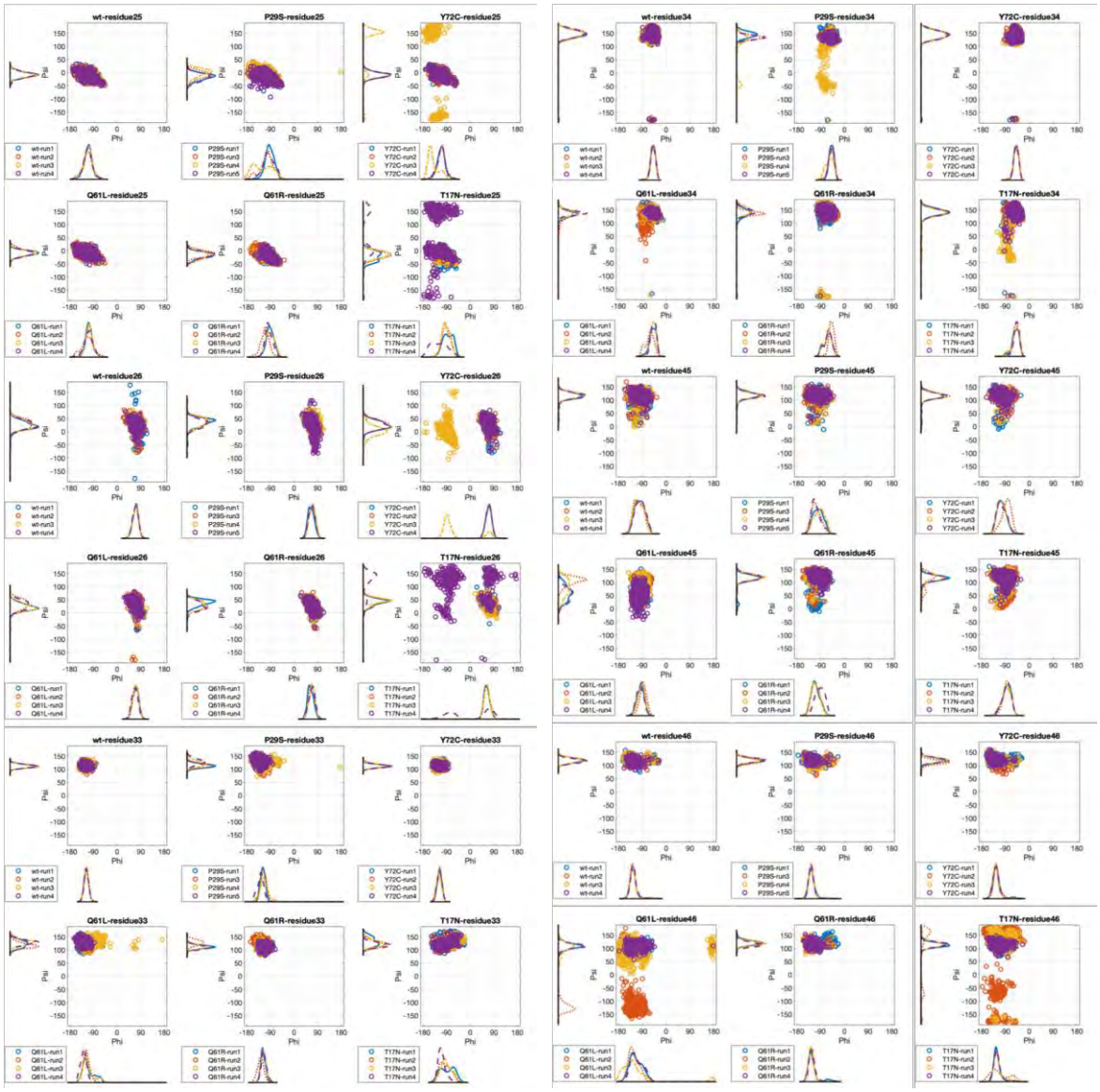

Figure S14. Backbone dihedral angle trajectories of the PAK1-binding residues during simulations. Only residues with distinctive behavior are shown.

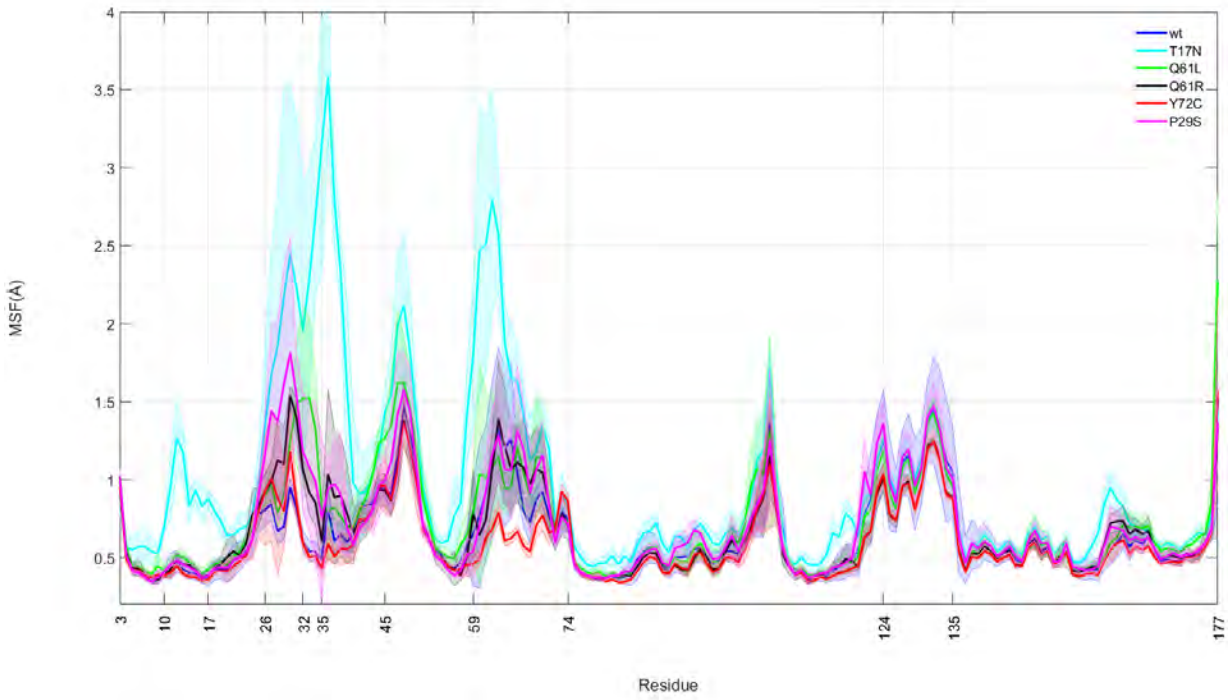

Figure S15. MSF profiles during parallel MD simulations for the wild-type and mutant Rac1 structures.

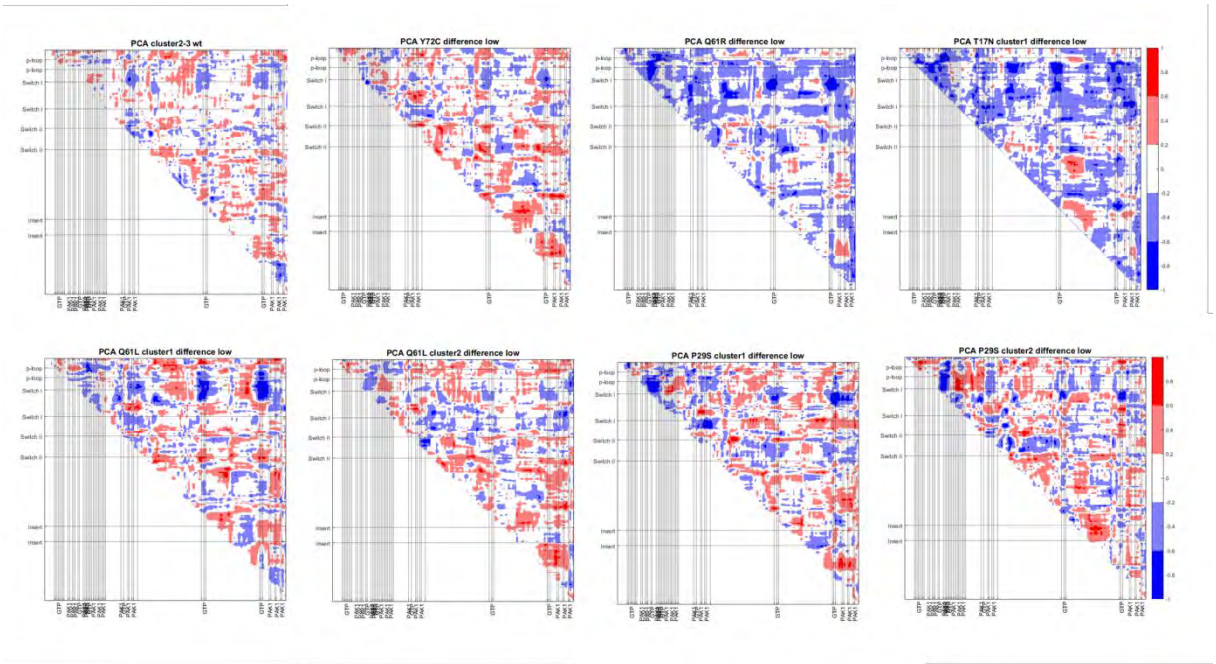

Figure S16. PCA difference of state 1 wt (cluster 2) and mutant clusters from the state 2 wt Rac1 (cluster 3).

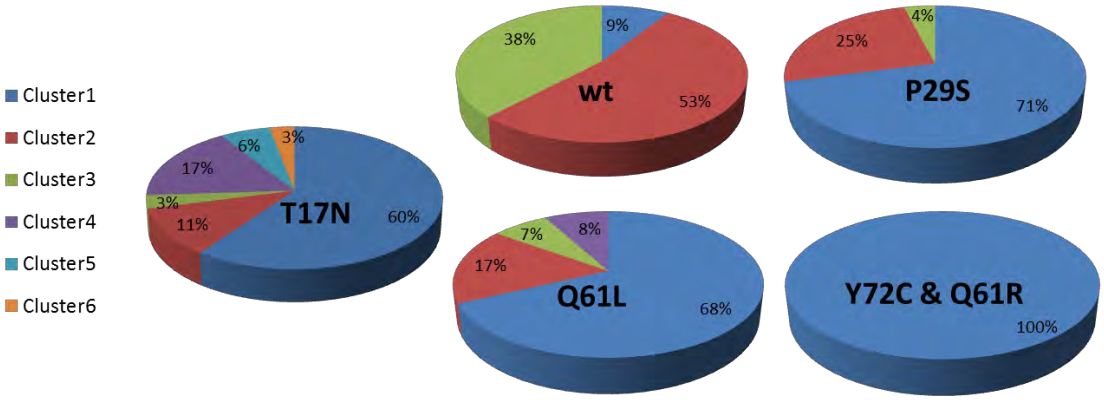

Figure S17. Distributions of Ensembles of Rac1 Conformations.

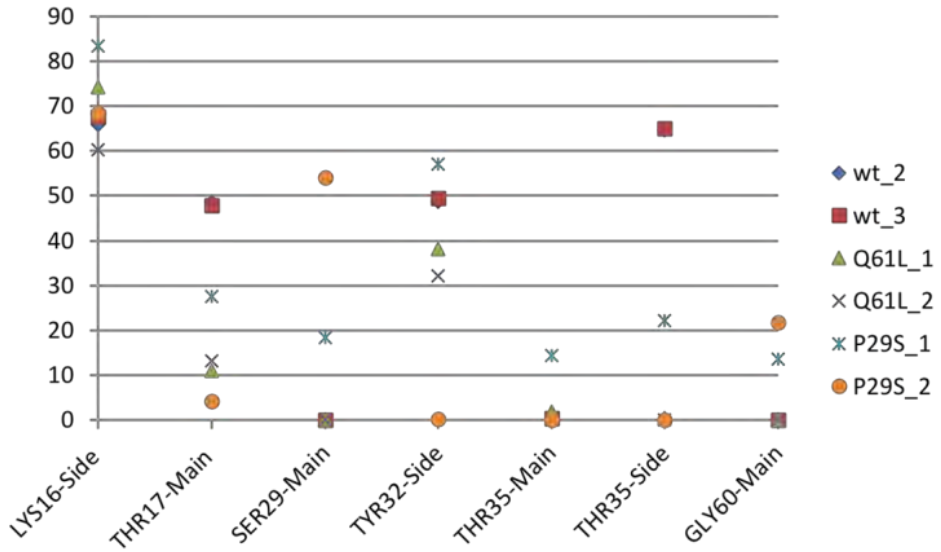

Figure S18. Rac1-GTP H-bonding occupancy changes with mutations, based on trajectories that are clustered into two or more groups.

Supporting Tables

Table S1. The details of the molecular-dynamics (MD) simulations.

# of Parallel Simulations	Structure (PDB ID)	Length (ns) of Each Parallel Simulation	Equilibration Time Interval (ns) of Each Parallel Simulation	Total Equilibration Time (ns) of Parallel Simulations
4	Rac1 wt structure (3th5)	100	4 – 5 – 20 – 15	356
4	Rac1 T17N Mutant (3b13)	100	20 – 5 – 5 – 20	350
4	Rac1 Q61L Mutant (4gzl)	100	(10-85) – (10-90) – 25 – (25-95)	300
4	Rac1 Y72C Mutant (*in silico*)	100	5 – 10 – 10 – (5-95)	365
4	Rac1 Q61R Mutant (*in silico*)	100	(10-85) – 25 – 20 – 15	315
4	Rac1 P29S Mutant (3sbd)	100	10 – (2-92) – 15 – (9-83)	339

Table S2. Ensembles of Rac1 conformations and binding properties of the modeled Rac1 (top ten cluster members) - PAK1 complexes.

CaseStudy_Cluster# _ member#	Global Binding Energy (unitless)	ΔG^{diss} (kcal/mol)	CaseStudy_Cluster# _ member#	Global Binding Energy (unitless)	ΔG^{diss} (kcal/mol)
wt_cluster2_1	-96.95	5.5	Q61L_cluster2_1	-85.85	8.2
wt_cluster2_2	-87.95	3.1	Q61L_cluster2_2	-76.65	6.7
wt_cluster2_3	-94.93	5.1	Q61L_cluster2_3	-62.98	5.4
wt_cluster2_4	-91.67	6.7	Q61L_cluster2_4	-87.19	6.8
wt_cluster2_5	-125.12	9.2	Q61L_cluster2_5	-65.18	8.4
wt_cluster2_6	-112.56	7.3	Q61L_cluster2_6	-114.69	8.1
wt_cluster2_7	-131.04	9.2	Q61L_cluster2_7	-96.33	5.6
wt_cluster2_8	-110.84	5.2	Q61L_cluster2_8	-74.51	4.3
wt_cluster2_9	-83.23	7.5	Q61L_cluster2_9	-89.55	6.1
wt_cluster2_10	-108.54	6.4	Q61L_cluster2_10	-112.47	8.3
wt_cluster3_1	-77.87	3.9	P29S_cluster1_1	-99.84	6.4
wt_cluster3_2	-97.64	8.5	P29S_cluster1_2	-83.27	3.7
wt_cluster3_3	-99.92	6.3	P29S_cluster1_3	-123.7	6.9
wt_cluster3_4	-107.64	7	P29S_cluster1_4	-67.72	4
wt_cluster3_5	-98.5	4.8	P29S_cluster1_5	-102.41	6.7
wt_cluster3_6	-71.58	1.3	P29S_cluster1_6	-109.14	5.5
wt_cluster3_7	-80.1	6.4	P29S_cluster1_7	-73.33	4.2
wt_cluster3_8	-104.76	5.3	P29S_cluster1_8	-116.96	6.6
wt_cluster3_9	-88.95	7	P29S_cluster1_9	-89.61	6.3
wt_cluster3_10	-104	6.7	P29S_cluster1_10	-101.11	5.5
Y72C_cluster1_1	-110.07	6.5	P29S_cluster2_1	-79.76	3.2
Y72C_cluster1_2	-91.73	5.9	P29S_cluster2_2	-99.46	10
Y72C_cluster1_3	-77.04	7.8	P29S_cluster2_3	-81.28	4
Y72C_cluster1_4	-103.76	5.7	P29S_cluster2_4	-87.87	3.6
Y72C_cluster1_5	-89.21	7.7	P29S_cluster2_5	-121.36	7.9
Y72C_cluster1_6	-106.04	8.2	P29S_cluster2_6	-55.57	-2.2
Y72C_cluster1_7	-108.08	8.2	P29S_cluster2_7	-78.01	3
Y72C_cluster1_8	-92.97	2.5	P29S_cluster2_8	-54.75	0.1
Y72C_cluster1_9	-58.77	2.7	P29S_cluster2_9	-89.55	3.2
Y72C_cluster1_10	-89.37	4.2	P29S_cluster2_10	-90.04	5.4
Q61R_cluster1_1	-87.06	4.1	T17N_cluster1_1	-66.4	7.3
Q61R_cluster1_2	-98.98	5.8	T17N_cluster1_2	-59.83	7.2
Q61R_cluster1_3	-98.21	6.1	T17N_cluster1_3	-33.98	-0.8
Q61R_cluster1_4	-97.62	6.2	T17N_cluster1_4	-57.89	1.6
Q61R_cluster1_5	-98.22	7.9	T17N_cluster1_5	-48.74	2.1
Q61R_cluster1_6	-85.98	4.9	T17N_cluster1_6	-33.82	-2
Q61R_cluster1_7	-96.97	5.1	T17N_cluster1_7	-35.07	-0.9

Q61R_cluster1_8	-92.24	5.6	T17N_cluster1_8	-36.01	3.7
Q61R_cluster1_9	-111.01	5.9	T17N_cluster1_9	-85.58	6.7
Q61R_cluster1_10	-124.99	7.3	T17N_cluster1_10	-57.58	5.7
Q61L_cluster1_1	-96.11	5			
Q61L_cluster1_2	-113.94	5.2			
Q61L_cluster1_3	-109.5	4.4			
Q61L_cluster1_4	-96.3	5.3			
Q61L_cluster1_5	-110.9	8.2			
Q61L_cluster1_6	-112.54	7.6			
Q61L_cluster1_7	-119.2	4.3			
Q61L_cluster1_8	-114.96	5.1			
Q61L_cluster1_9	-107.64	6.8			
Q61L_cluster1_10	-77.41	3.1			

Table S3. Mean side chain conformational angles (Chi1).

Residue ID	wt (in °)	Y72C (in °)	P29S (in °)	Q61R (in °)	Q61L (in °)	T17N (in °)
T17	321±8	321±8	300±28	300±11	308±11	203±97
T35	302±8	302±8	286±35	289±9	248±90	143±88
V36	180, 300	180		300	180	
F37	180	180	180, 300	180, 300	180, 60	
Y64	2 states	1 state	1 state	1 state	1 state	
L67	180, 300	300	180, 300	180, 300	180, 300	180, 300

Supporting References

1. Hutter JL & Bechhoefer J (1993) Calibration of atomic-force microscope tips. *Rev. Sci. Instrum.* 64(7):1868–1873.
2. Evans E & Ritchie K (1997) Dynamic strength of molecular adhesion bonds. *Biophysical journal* 72(4):1541-1555.
3. Bell GI (1978) Models for the specific adhesion of cells to cells. *Science* 200(4342):618-627.
4. Bahar I & Jernigan RL (1998) Vibrational dynamics of transfer RNAs: comparison of the free and synthetase-bound forms. *Journal of molecular biology* 281(5):871-884.
5. Haliloglu T, Bahar I, & Erman B (1997) Gaussian dynamics of folded proteins. *Physical Review Letters* 79:3090.
6. Emekli U, Schneidman-Duhovny D, Wolfson HJ, Nussinov R, & Haliloglu T (2008) HingeProt: automated prediction of hinges in protein structures. *Proteins* 70(4):1219-1227.
7. Oliphant TE (2007) Python for Scientific Computing. *Computing in Science & Engineering* 9(10).
8. Forbes SA*, et al.* (2008) The Catalogue of Somatic Mutations in Cancer (COSMIC). *Current protocols in human genetics / editorial board, Jonathan L. Haines ... [et al.]* Chapter 10:Unit 10 11.
9. Gao J*, et al.* (2013) Integrative analysis of complex cancer genomics and clinical profiles using the cBioPortal. *Science signaling* 6(269):pl1.
10. Cerami E*, et al.* (2012) The cBio cancer genomics portal: an open platform for exploring multidimensional cancer genomics data. *Cancer discovery* 2(5):401-404.
11. Humphrey W, Dalke A, & Schulten K (1996) VMD: visual molecular dynamics. *Journal of molecular graphics* 14(1):33-38, 27-38.
12. Brooks BR*, et al.* (1983) CHARMM: A program for macromolecular energy, minimization, and dynamics calculations. *Journal of computational chemistry* 4:187-217.
13. Phillips JC*, et al.* (2005) Scalable molecular dynamics with NAMD. *Journal of computational chemistry* 26(16):1781-1802.
14. Levy RM, Karplus M, & McCammon JA (1979) Diffusive Langevin dynamics of model alkanes. *Chemical Physics Letters* 65:4-11.
15. Ryckaert JP, Ciccotti G, & Berendsen HJC (1977) Numerical integration of the cartesian equations of motion of a system with constraints: molecular dynamics of< i> n</i>-alkanes. *J Comput Phys* 23(327-341).
16. Jorgensen WL (1983) Comparison of simple potential functions for simulating liquid water. *Journal of the American Chemical Society* 103:335-340.
17. Darden T, York D, & Pedersen L (1993) Particle mesh Ewald: An N· log (N) method for Ewald sums in large systems. *The Journal of chemical physics* 98:10089-10092.
18. Tuncbag N, Gursoy A, Nussinov R, & Keskin O (2011) Predicting protein-protein interactions on a proteome scale by matching evolutionary and structural similarities at interfaces using PRISM. *Nature protocols* 6(9):1341-1354.
19. Baspinar A, Cukuroglu E, Nussinov R, Keskin O, & Gursoy A (2014) PRISM: a web server and repository for prediction of protein-protein interactions and modeling their 3D complexes. *Nucleic acids research* 42(Web Server issue):W285-289.
20. Mashiach E, Nussinov R, & Wolfson HJ (2010) FiberDock: a web server for flexible induced-fit backbone refinement in molecular docking. *Nucleic acids research* 38(Web Server issue):W457-461.
21. Krissinel E & Henrick K (2007) Inference of macromolecular assemblies from crystalline state. *Journal of molecular biology* 372(3):774-797.
22. Porter AP, Papaioannou A, & Malliri A (2016) Deregulation of Rho GTPases in cancer. *Small GTPases* 7(3):123-138.